A three dimensional kinetic Monte Carlo model for simulating the carbon/sulfur mesostructural evolutions of discharging lithium sulfur batteries

Vigneshwaran Thangavel, Oscar Xavier Guerrero, Matias Quiroga, Adelphe Matsiegui Mikala, Alexis Rucci, Alejandro A. Franco

Version of Record: https://www.sciencedirect.com/science/article/pii/S2405829719308712
Manuscript_b44a706627d22f612fa85339ddc9afd7

A three dimensional kinetic Monte Carlo model for simulating the carbon/sulfur mesostructural evolutions of discharging Lithium sulfur batteries

Vigneshwaran Thangavel,[a,b] Oscar Xavier Guerrero,[c] Matias Quiroga,[a,b,d] Adelphe Matsiegui Mikala,[a,b] Alexis Rucci[a,b] and Alejandro A. Franco[a,b,e,f,*]

[a]Laboratoire de Réactivité et Chimie des Solides (LRCS), CNRS UMR 7314, Université de Picardie Jules Verne, Hub de l'Energie, Rue Baudelocque, 80039 Amiens Cedex, France.

[b]Réseau sur le Stockage Electrochimique de l'Energie (RS2E), FR CNRS 3459, Hub de l'Energie, Rue Baudelocque, 80039 Amiens Cedex, France.

[c]Departamento de Química, CINVESTAV, Av. Instituto Politécnico Nacional 2508, Col. San Pedro Zacatenco, Delegación Gustavo A. Madero, C.P 07360, Ciudad de México, México.

[d]Instituto de Física de Materiales Tandil - IFIMAT (UNCPBA) and CIFICEN (UNCPBA CICPBA-CONICET), Pinto 399, (7000) Tandil, Argentina.

[e]ALISTORE-ERI, European Research Institute, FR CNRS 3104, Hub de l'Energie, Rue Baudelocque, 80039 Amiens Cedex, France.

[f]Institut Universitaire de France, 103 Boulevard Saint Michel, 75005 Paris, France.

*Corresponding author: alejandro.franco@u-picardie.fr

A three dimensional kinetic Monte Carlo model for simulating the carbon/sulfur mesostructural evolutions of discharging Lithium sulfur batteries

ABSTRACT

The carbon/sulfur composite cathodes of lithium sulfur batteries undergo mesostructural evolutions during discharge due to the precipitation/dissolution reactions of solid sulfur and Li_2S. Furthermore, the cathode design and discharge parameters also impact the mesostructural evolutions of carbon/sulfur composites. In order to compare and study these mesostructural evolutions, we have developed a novel three dimensional kinetic Monte Carlo (kMC) model based on an algorithm called Variable step size method (VSSM). Our model describes mechanisms such as reactions and diffusions of different polysulfides, dissolution of solid sulfur and electrodeposition of Li_2S. The initial carbon/sulfur mesostructure used in our model is created based on its desired structural and geometric properties using an *in-silico* method. In this paper, we present the theoretical development of our kMC model and demonstrate its capabilities using discharge simulations of a model carbon/sulfur mesostructure under two different rates (C-rates) namely C/2 and 2C. Furthermore, we also present the impact of initial $S_{8(s)}$ loading on the 2C discharge simulation.

Keywords: Lithium sulfur batteries, carbon/sulfur mesostructures, cathode mesostructural evolutions, kinetic Monte Carlo model, stochastic modeling, discharge simulations.

1. Introduction

Li-ion batteries (LIBs) are currently used to power electric vehicles (EVs). However to enhance their driving ranges, [1] development of next generation of batteries with high specific capacities and energy densities are carried out [2]. Lithium sulfur (Li-S) batteries constitute a promising technology among them, due to its viability [3], cheapness, abundance of materials [4] and very high theoretical energy density (2570 Wh/Kg of solid sulfur in the cathode) [5].

The cathodes of conventional Li-S batteries are carbon/sulfur (C/S) composites, where the inert carbon in the cathode exists as an electron conducting porous matrix which holds solid sulfur and electrolyte, whereas Li-metal foil is used as anode [6–8]. Unlike Li-ion batteries, the cathode of the Li-S batteries undergoes significant mesostructural changes during discharge due to its unique operational mechanism.

During discharge, the solid sulfur in the cathode dissolves and undergoes multiple subsequent reduction reactions producing solvated polysulfide intermediates in the electrolyte and precipitation of Li_2S over the carbon surface [9,10]. The morphology of the Li_2S precipitates depends on the operation and cathode designs such as discharge rate, sulfur loading, etc. [11,12]. Since these Li_2S precipitates are insulating they impact the discharge performance due to phenomena such as surface passivation [13] and pore-clogging [14].

Due to the complicated nature of its operating principles, different phenomena of Li-S battery cathode are often assessed using mathematical models.[15,16] Continuum Li-S batteries models have been useful in identifying different performance limitations. However, most of them only consider the effective cathode structural properties and thereby they overlook the three-dimensional nature of the C/S mesostructure and the Li_2S deposits. [17–21] Recently, Ren *et al.* developed a one-dimensional continuum discharge model incorporating nucleation and growth dynamics which predicts the particle size distributions of Li_2S precipitates that are dependent on the discharge rate [22]. Furthermore, Mistry *et al.* developed a modeling framework where the precipitates are grown on three-dimensional porous carbon microstructures based on deposition energy and a morphology parameter [23]. They have also calculated the effective cathode structural evolutions of those microstructures and incorporated them in their continuum discharge model to predict the impact of Li_2S morphologies, sulfur

loadings, etc. on the performance. Contrary to the aforementioned continuum models, Beltran *et al.* developed a classical reactive molecular dynamics model which explicitly simulates the discharge of a three dimensional (3D) graphene/sulfur microstructure [24]. This model is capable of predicting the reduction of sulfur, interactions between different atoms, discharge potential and volume expansion of graphene/sulfur microstructures upon on lithiation. However, it does not provide details about the mesostructural evolutions such as porosity, coverage of Li_2S precipitates on carbon, etc.

Kinetic Monte Carlo (kMC) models have been adopted in recent years to predict the mesostructural evolutions of next-generation batteries such as Li-O_2, slurry redox flow batteries, etc. [25–27]. In the context of Li-S batteries, Liu *et al.* developed a kMC model which includes phenomena such as adsorption, desorption and surface diffusion of Li_2S over a flat carbon substrate to predict the impact of temperature, S^{2-} concentration, etc. on the mesoscale deposition of Li_2S [28]. Although this model provides details about the mesoscale evolutions of Li_2S deposition such as coverage, thickness, etc. it cannot be used to study the direct impact of the discharge on the deposition. Since this aforementioned model does not consider any electrochemical reduction process. Therefore, we have developed a 3D kMC model which explicitly simulates structural the evolutions C/S mesostructure and Li_2S precipitation during discharge. Our model includes phenomena such as dissolution reaction of solid sulfur, diffusions and reduction reactions of solvated sulfur and polysulfides and electrodeposition of Li_2S. The main objective of this paper is to present the development our kMC model as a methodology towards the understanding Li-S discharge process at every scale. In the theoretical methodology section, we will first introduce our *in-silico* method to create the model C/S mesostructure (subsection 2.1), following which we will discuss the kMC algorithm called Variable Step Size Method (VSSM) used in our model along with the equations for rate constants of different phenomena and the assumptions (subsection 2.2). In the results and

discussions section, we will present the visualization and quantification of the general observables of the discharge simulations for two different C-rates (subsection 3.1). Furthermore, we will also discuss the post-processed results generated by the computational tools such as radial distribution function and cluster recognition algorithm. These results are used to compare the impact of the discharge rate on the mesoscale deposition of Li_2S over the carbon surface (subsection 3.2). Finally, the impact of initial $S_{8(s)}$ loading on the 2C discharge simulation is presented in the subsection 3.3.

2. Theoretical methodology

2.1 Creation of initial C/S mesostructure

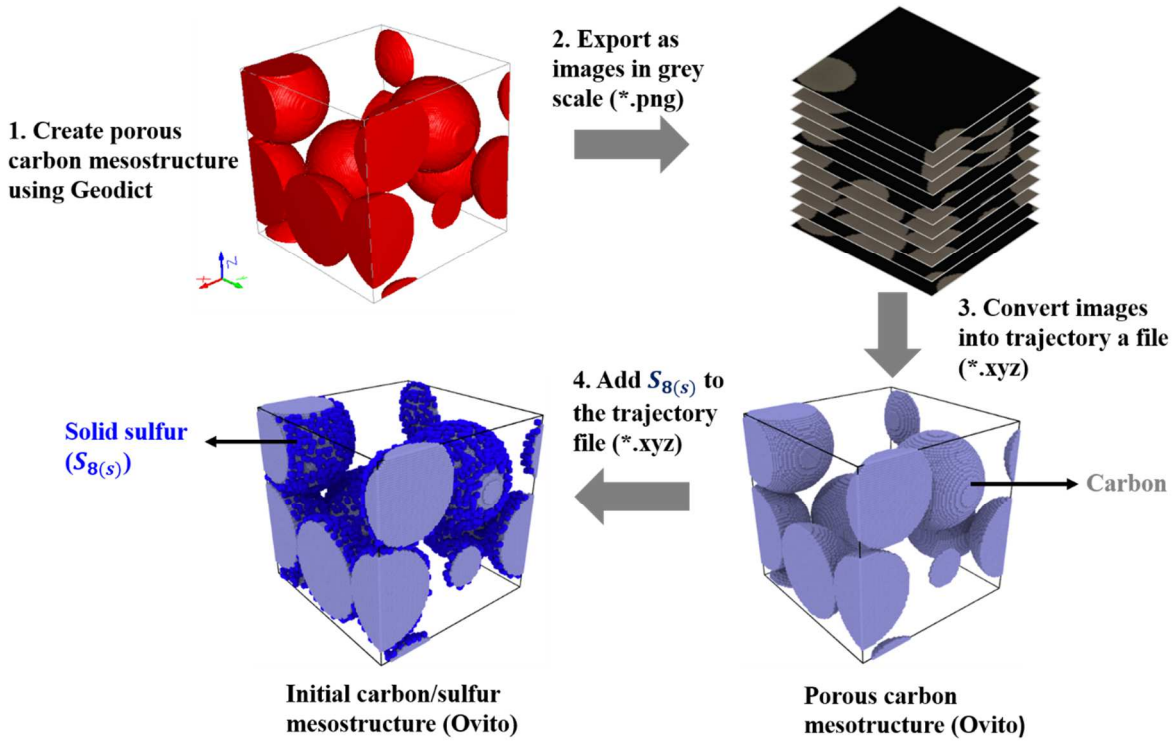

Figure 1. Schematics of our *in-silico* method to create the initial C/S mesostructure.

In this paper, we have formalized an *in-silico* method to create a 3D simulation box based on the structural and geometric properties of the desired initial C/S mesostructure used in our kMC

model (Figure 1). Initially, a cubic box containing randomly distributed spherical carbon particles representing the porous carbon mesostructure was created using a commercial software called Geodict. The sensitivity to the variation in the random distribution of spherical carbon particles is discussed in the subsection S4.1 of the supporting information. The side length of this cubic box and the diameter of the carbon particles were set to 50 and 25 nm respectively. The porosity of the entire mesostructure was set to 67%. The cubic box was then meshed along each side into 100 cubic volumetric elements called voxels. The side length of each voxel was set to 5 Å which is close to the S-S bond length (4.1 Å) in an isothermally stabilized graphene/S microstructure [24], and therefore it was set as the resolution between S atoms. The resulting structure was exported as a stack of images (*.png). An *in-house* developed python code uses the grey scale values of these images to create the simulation box with voxels containing carbon atoms. Locations of the carbon atoms in the simulation box were exported to a trajectory file (*.xyz) along with those of the solid sulfur ($S_{8(s)}$) particles (Figure 1). The visualizations in this work were done using the open source software Ovito [29].

The locations of each carbon (C) and sulfur (S) atoms in $S_{8(s)}$ were identified using the integer numbers 1 and 2. The $S_{8(s)}$ particles were randomly distributed next to the C atoms at the carbon particle surface since the impregnated $S_{8(s)}$ sticks to the surface of the carbon particles [6]. Furthermore, the mass ratio between C and S atoms was set to 1:0.27. We have used this low sulfur loading in our simulations to reduce the computational cost.

Finally, the resulting trajectory file is read by our *in-house* developed kMC python code, which reconstructs the simulation box and utilizes it as the initial C/S mesostructure. It should be noted that our *in-silico* C/S mesostructure creation method and kMC code are not specific to the aforementioned dimensions, structural and geometric parameters. In fact, we can customize the initial C/S mesostructure by changing the parameters such as of the shape and size of the carbon particles, mesostructure porosity, sulfur loading, etc. In the future, this *in-silico* method

will also be used to transform the tomographic images of a real C/S composite electrode into a simulation box which will then be used as the initial C/S mesostructure of our kMC code. Although the carbon mesostructure presented here is not tied to a direct tomographical measurement, its continuum-level descriptors are relevant with the previously reported carbon host materials. Ma *et al.*, utilized cauliflower like carbon/sulfur composite cathode material, in which the size of the carbon particles is 25 nm.[30] The volume percentage of the pores in their cathode material with sizes above 20 nm is 63% which is closer to the porosity of the mesostructure (0.67) presented in our manuscript. Zheng *et al.*, used Acetylene Black (AB) carbon nanoparticles in the cathode whose surface area is 123.6 $m^2.g^{-1}$, [31] which is closer to that of our mesostructure (133.3 $m^2.g^{-1}$, calculation given in Supporting information).

2.2 Development of our kMC-VSSM model and its assumptions

In the past, an on-lattice kMC algorithm called VSSM was utilized to describe the reaction and diffusion events in Fuel cells [32] and Li-O_2 batteries [25,26] and Brownian motion of suspended particles in slurry redox flow batteries [27,33]. Here, we have adopted a similar method to select and execute the reaction and diffusion events (Figure 2) during the discharge simulation of an *in-silico* created C/S mesostructure (Figure 1).

The reaction events considered in our kMC model are as follows,

$$S_{8(s)} \rightarrow S_{8(l)} \tag{1}$$

$$S_{8(l)} + 4e^- \rightarrow 2S_{4(l)}^{2-} \tag{2}$$

$$S_{4(l)}^{2-} + 2e^- \rightarrow 2S_{2(l)}^{2-} \tag{3}$$

$$S_{2(l)}^{2-} + 4Li^+ + 2e^- \rightarrow 2Li_2S_{(s)} \tag{4}$$

where, Eq. 1 is the chemical dissolution of $S_{8(s)}$ to solvated $S_{8(l)}$ and Eqs. 2 and 3 are the electrochemical reduction reactions of solvated $S_{4(l)}^{2-}$ and $S_{2(l)}^{2-}$ respectively. Finally, Eq. 4 is the

electrodeposition of solid $Li_2S_{(s)}$. Although there could be several reactions involving multiple solvated polysulfide species that occur during the operation of Li-S batteries, here we consider only this reduced set of reaction steps (eqs. 1-4) in order to limit the computational costs of our simulations and complexities arising through multiple unknown parameters. This approximation is common in many previously reported Li-S batteries models [19,34–37].

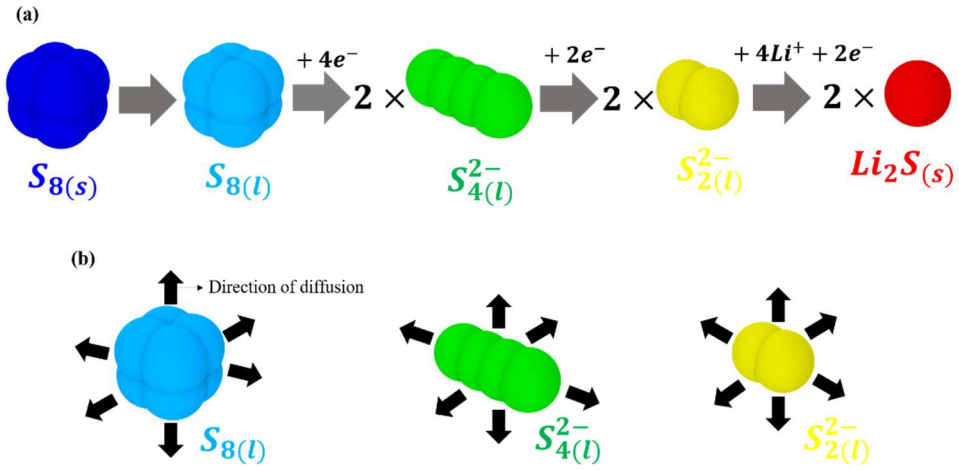

Figure 2. Schematic representations, of (a) the reaction events considered in our model along with the coarse-grained structures of the different types sulfur based particles and (b) the six directions in which the solvated particles ($S_{8(l)}$, $S^{2-}_{4(l)}$ and $S^{2-}_{2(l)}$) can be diffuse.

Similar to S in $S_{8(s)}$ particles, atoms in $S_{8(l)}$, $S^{2-}_{4(l)}$, $S^{2-}_{2(l)}$ and $Li_2S_{(s)}$ particles are also identified using unique set of integer numbers namely 3, 4, 5 and 6 respectively. The coarse-grained structures of the different sulfur based particles along with the schematic representation of the reaction events between them and the directions in which the solvated particles can diffuse are shown in Figure 2. Among the reactions considered in our model (Eq. 1-4), only the Li_2S electrodeposition involves solvated $Li^+_{(l)}$ in the electrolyte. Moreover, the $Li^+_{(l)}$ concentration in Li-S batteries electrolyte is much larger (≈1000–5000mM) than that of $S^{2-}_{2(l)}$ (≈10 mM) [17], therefore the kinetics of Li_2S electrodeposition will primarily depend on the latter. Since the

solvated $Li^{+}_{(l)}$ and anion of Li salt are highly concentrated in the electrolyte, the probilities of our kMC model selecting their diffusion events are much higher. This will ultimately increase the simulation cost. Therefore, the Li salt containing supporting electrolyte is not explicitly considered in our model, and we assume that they are uniformly distributed in the void volume of the simulation box.

2.2.1 Equations for rate constants of different types of events

According to the VSSM algorithm used in our KMC model, an event is selected and executed in a given time step or an iteration based on the weighted probabilities of all the possible events which depend on their corresponding rate constants. Therefore, it is important to determine the rate constants for different types of events.

The rate constants of the electrochemical reactions in our model (eqs. 2-4) could be calculated using Butler Volmer type equations [25,26]. However, the over potentials in the Butler Volmer equations vary a lot during the discharge of Li-S batteries [38]. Since we intend to simulate the discharge of our *in-silico* created C/S mesostructure under a galvanostatic condition, we have derived the rate constants of the electrochemical reactions based on the discharge current (I) which remains constant at any given time. Therefore, the kinetic rate constant (K_j^{ele}) of an electrochemical reaction (j) is given by a Faraday's law type equation,

$$K_j^{ele} = \frac{I}{n_j q_e}\Theta(\delta_e) \tag{5}$$

The discharge current I is determined from the discharge C-rate and initial mass of $S_{8(s)}$ present inside simulation box. n_j and q_e in eq. 5 are the number of electrons transferred in an electrochemical reaction (j) and the charge of the electron respectively. According to eq. 5, the applied current is equal to the Faradaic current at each iteration. Neidhardt *et al.*, implemented double layer phenomenon in their continuum Li-S batteries model. We neglected this

phenomenon in our kMC model, since its impact on the simulated results and mechanisms in the Li-S batteries are still unclear. Implementation of double layer dynamics would increase the computational cost of our model, since it would require us to simulate the supporting electrolyte explicitly or coupling the KMC model with a physical double layer model. We intend to work on this implementation in the future.

In order for the electrochemical reactions to occur, the solvated polysulfides should be present within the electron tunnelling distance (δ_e) from the carbon surface and the electron tunnelling probability ($\Theta(\delta_e)$) is given by a simple function [25],

$$\Theta(\delta_e) = \begin{cases} 1, & 0 \leq \delta_e \leq 10\ nm \\ 0, & \delta_e > 10\ nm \end{cases} \quad (6)$$

Furthermore, the kinetic rate constant of the $Li_2S_{(s)}$ deposition reaction is considered only when the $S^{2-}_{2(l)}$ particles are present next to either a carbon atom or a $Li_2S_{(s)}$ particle. This condition mimics the nucleation and growth processes of $Li_2S_{(s)}$ observed in Li-S batteries. In few chronoamperometric investigations of $Li_2S_{(s)}$ electrodeposition, [39,40] A. Beweick, M. Fleischman, and H.R. Thirsk (BFT) model [41,42] and Scharifker-Hills (SH) Model were used fit the dimensionless current signals. These models assume that the charge transfer step of the electrodeposition is fast and the growth Li_2S nuclei are controlled by mass transport of solvated species to the electrode surface. However the model developed by Ren *et al.,* uses a modified Tafel equation to calculate current for the growth of Li_2S nuclei, [37] which is the rate of charge transfer step. Similarly, we have assumed that the nucleation and growth Li_2S are controlled by the charge transfer steps.

The sensitivity of the tunnelling distance (δ_e) on the 2C discharge simulation results are discussed in the supplementary information.

Since the electronic conductivities of solid $S_{8(s)}$ and $Li_2S_{(s)}$ are quite low [43], we have neglected them in our model. However, the inclusion of electronic transport rates within the solid deposits could be further improvement to our model and it will be carried out in the future.

As mentioned before, our model also considers the diffusion of solvated particles such as $S_{8(l)}$, $S_{4(l)}^{2-}$ and $S_{2(l)}^{2-}$ along six directions (Figure 2). The diffusion rate constant of a solvated particle (i) is given by the Stokes-Einstein's equation,

$$K_i^{dif} = \frac{\kappa_B T}{6\pi\eta r_i z^2} \tag{6}$$

where η and r_i are the viscosity of the electrolyte and radius of gyration of a solvated particle (i) respectively (see Table S1 in the supporting information). z is the distance displaced by the solvated particle along a given direction.

Since our model simulates the redox reaction of the solvated particles in the electrolyte phase near the electrode surface instead of solid-state-like reactions, [44] the ionic transport events through $S_{8(s)}$ and $Li_2S_{(s)}$ deposits [43] are neglected.

2.2.2 Working principle of our kMC-VSSM code

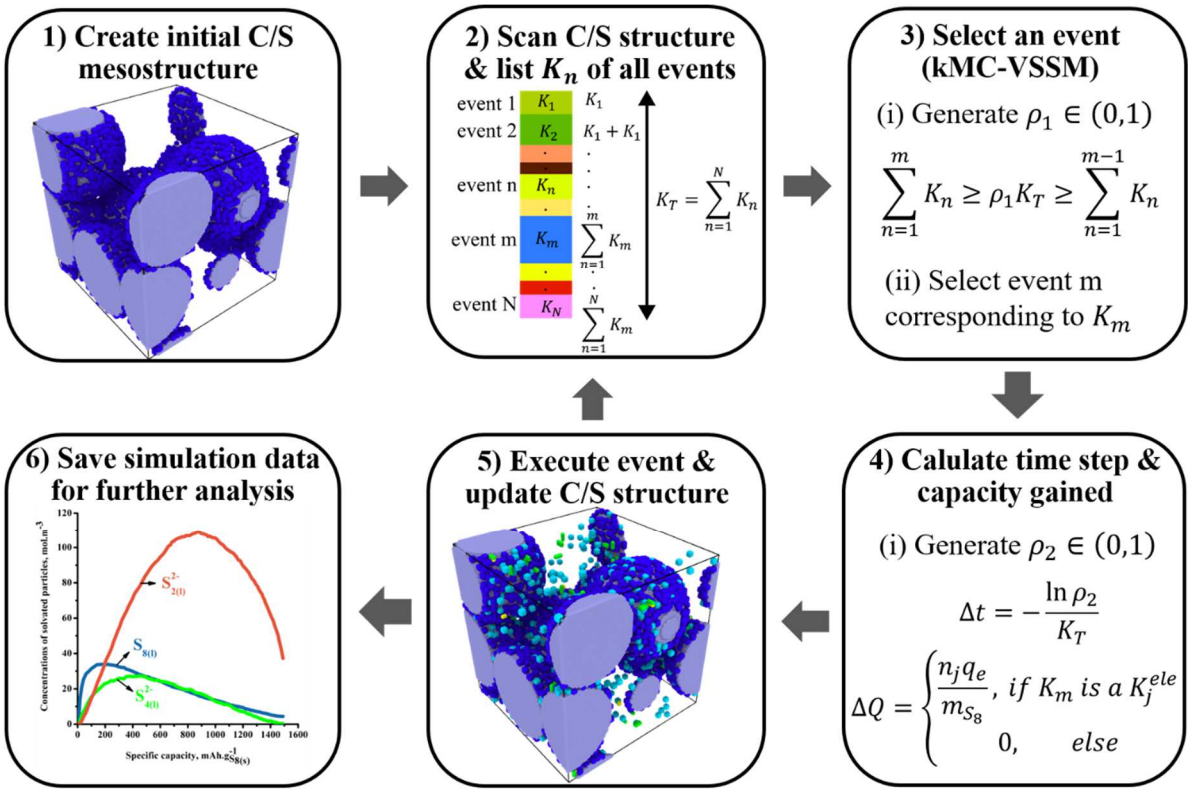

Figure 3. Workflow of our kMC-VSSM code.

Reconstruction of the simulation box containing our *in-silico* C/S mesostructure, is the initial step of our model (Figure 3), after which the kMC code enters into an iterative loop to execute the reaction and diffusion events during discharge simulation. In any given iterative cycle, the entire simulation box is initially scanned in order to find all the different types of particles and the possible events which could be performed by them. A list containing all the possible events is then stored in the computer memory, along with their corresponding particle types, individual and cumulative sums of rate constants, current and final locations inside the simulation box. After this step, the sum of all the possible events (K_T) is calculated as follows,

$$K_T = \sum_{n=1}^{N} K_n \tag{7}$$

where N is the total number of all the possible events in a given iterative cycle and K_n is the rate constant of nth event in the aforementioned list. K_n could be either a rate constant of a diffusion (k_i^{dif}) or a chemical (k_k^{che}) or an electrochemical reaction event (k_j^{ele}).

After calculating K_T, a pseudo random number (ρ_1) $\in (0,1)$ is generated. According to the conditional algorithm of our kMC-VSSM model – an event is selected based on the cumulative sums of the rate constants of all the possible events and the product of ρ_1 and K_T as follows,

$$\sum_{n=1}^{m} K_n \geq \rho_1 K_T \geq \sum_{n=1}^{m-1} K_n \tag{8}$$

where m is the number of the selected event in the list. According to the condition above (Eq. 8), in any given iterative cycle, the events with large rate constants have larger probabilities to be selected. Since diffusion rate constants are normally larger than electrochemical rate constants, our kMC code has to go through a large number of iterative cycles which select diffusion events before an electrochemical reaction event is selected. Therefore, in each iterative cycle, we only consider the diffusion rates of solvated particles which could be displaced to a particular distance along anyone of the six directions within the simulation box. This criterion will increase the frequency in which electrochemical events are selected, and thereby it aids the discharge simulation to progress faster.

Following the event selection process of an iterative cycle, its corresponding time step (Δt) is calculated as follows,

$$\Delta t = -\frac{\ln \rho_2}{K_T} \tag{9}$$

where ρ_2 is the second pseudo random number $\in (0,1)$. Since Δt is inversely proportional to K_T, it varies from one iterative cycle to another and it also makes the calculated time (t) after each iteration to be low. However, since we are interested in comparing the simulated results

of two different discharge rates, it is much more relevant to represent them as functions of specific capacity (Q). Therefore, we also calculate the specific capacity gained (ΔQ) during each iteration using the following equation,

$$\Delta Q = \begin{cases} \dfrac{n_j q_e}{m_{S_{8(s)}}}, & if\ K_m\ is\ a\ K_j^{ele} \\ 0, & else \end{cases} \quad (10)$$

where the product of n_j and q_e in Eq. 10 is the charge transferred during the selected electrochemical event (j) and $m_{S_{8(s)}}$ is the initial mass of $S_{8(s)}$ present in the simulation box.

The final step in the iterative loop our kMC code is the execution of the selected event and the evolution of the C/S mesostructure inside the simulation box. This evolved C/S mesostructure, once again goes through another subsequent cycle consisting of steps such as scanning to find all possible events, selection and execution of an event and evolution C/S mesostructure. After a selected amount of cycles of this iterative process, the details of the simulation box such as number and locations of different types of particles, specific capacity, time and porosity are saved for further analysis. Discharge simulations can go on for several days and they are stopped either when all the $S_{8(S)}$ and solvated sulfur based particles are converted to $Li_2S_{(s)}$ or if they have been running for too long with very few changes in the type of sulfur particles inside the simulation box. .

3. **Results and discussions**

In this section, we have presented the discharge simulation results for two different C-rates namely C/2 and 2C. The same initial C/S mesostructure created using our *in-silico* method (presented in subsection 2.1) – was used for both the simulations. The C/2 and 2C discharge simulations were concluded *ad hoc* at 1230 and 1400 $mAh.g_{S_{8(s)}}^{-1}$ respectively. Around these capacities – diffusion events dominated over reaction events, resulting in very few changes in the types of sulfur based particles inside the simulation box. However, the results produced

using these simulations were still used to compare the impact of C-rates on the evolutions inside the C/S mesostructure. Furthermore, we also presented the 2C discharge simulation results of a mesostructure 1:0.54 C/S mass ratio and compared them with those of the 1:0.27 C/S mass ratio in order to investigate the sensitivity of our kMC model to the initial solid *S* loading. Due to the stochastic nature of our kMC model, each of these simulations were carried out three times to determine the confidence region which presented as shaded regions or error bars.

3.1 General effective evolutions of C/S mesostructure

As mentioned in the subsection 2.2.2, the locations of the different types of sulfur based particles after a selected number of cycles during the discharge simulation are saved in a trajectory file. This file can be used to track and visualize the evolution of the simulation (see video in the supplementary materials). The visualization of the simulation box could be done even when the simulation is performing. Figure 4, shows the visual evolution of the mesostructure inside the simulation box at different depths of discharge (DoDs) or specific capacities, during the 2C discharge simulation.

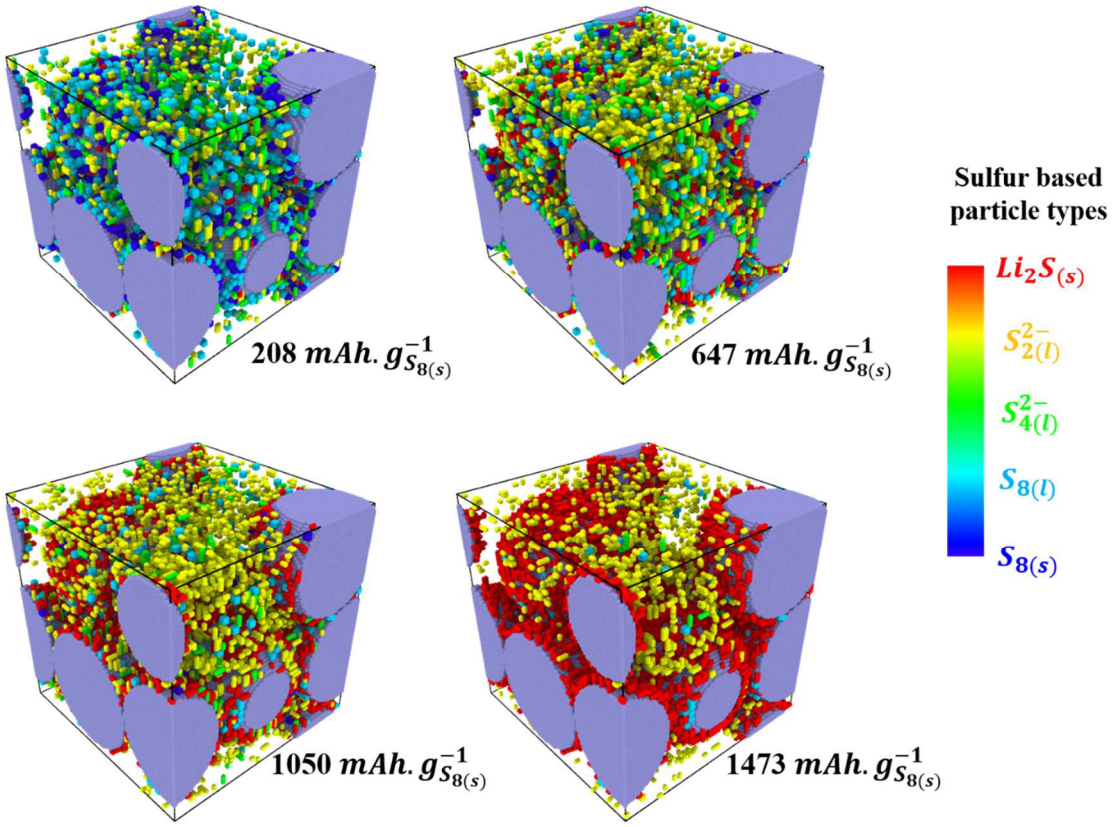

Figure 4. Visualization of the simulation box at 208, 647, 1050 and 1473 $mAh.g^{-1}_{S_{8(s)}}$ during the 2C discharge simulation. The colour map in the image shows the colour coding assigned to different types of sulfur based particle types, where $S_{8(s)}$, $S^{2-}_{8(l)}$, $S^{2-}_{4(l)}$, $S^{2-}_{2(l)}$ and $Li_2S_{(S)}$ particles are shown in navy blue, sky blue, green, yellow and red respectively.

When the simulation box is visualized, each type of sulfur based particle is assigned a unique colour (Figure 4). Therefore, it is possible to visually get an idea about the DoD of the simulation just from the colours of the particles inside the simulation box (Figure 4). Furthermore, this colour coding visually aids us to see the different types of events taking place inside the simulation box at different DoDs. In addition to visualization, the quantification of the different types of particles in the simulation box can be used to predict the effective properties such as concentrations of solvated particles, porosity of the mesostructure, etc.

The concentration of a solvated particle (c_i) inside the porous volume of C/S mesostructure is determined using the equation,

$$c_i = \frac{N_i}{N_A \epsilon V} \tag{11}$$

where N_A and N_i respectively are the Avogadro's number and the total number of solvated particles of type i (i.e. $S_{8(l)}$ or $S_{4(l)}^{2-}$ or $S_{2(l)}^{2-}$). V is the total volume of the simulation box and ϵ is the porosity of the C/S mesostructure, which is determined from the fraction between the number of voxels which are unoccupied by the atoms of solid particles (such as carbon, S_8 and Li_2S particles) and the total number of voxels in the simulation box.

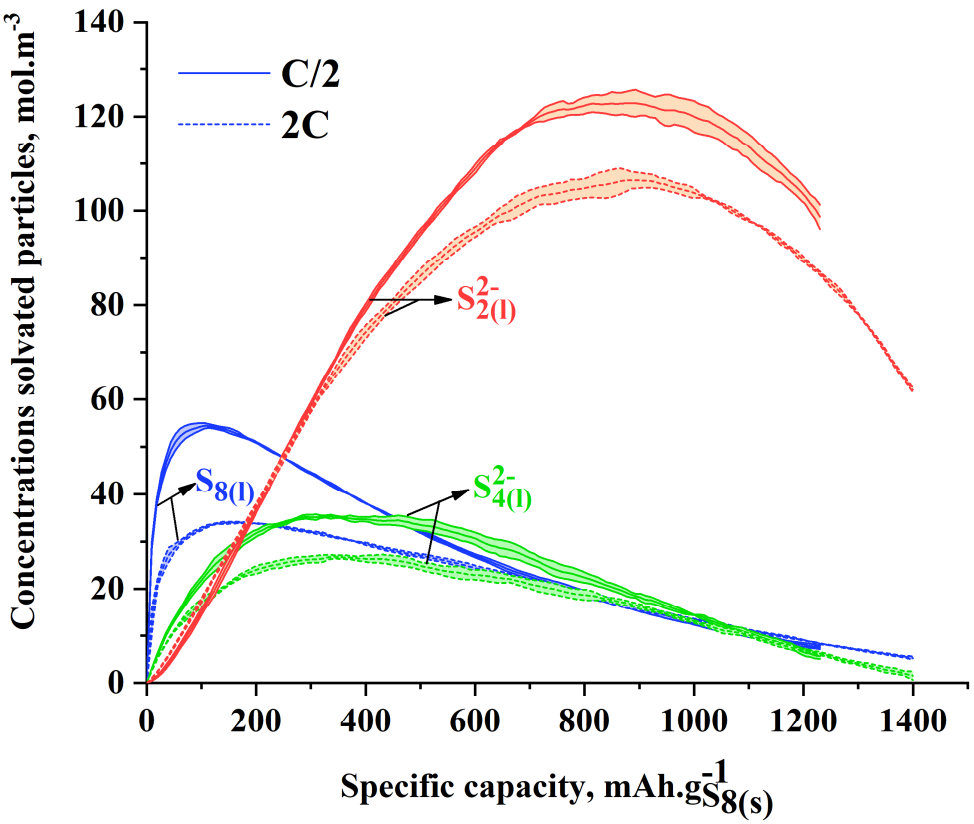

Figure 5. Evolutions of the concentrations of $S_{8(l)}$ (sky blue lines), $S_{4(l)}^{2-}$ (green lines) and $S_{2(l)}^{2-}$ (orange lines) during C/2 (solid lines) and 2C (dashed lines) discharge simulations.

Since the rate constants of the electrochemical reactions increase with the C-rates, the solvated particles during the fast discharge are consumed faster. Therefore, the concentrations of all the solvated particles during 2C discharge simulation are always lower than those of the C/2 (Figure 5). The evolutions of concentrations of different solvated particles (Figure 5) and numbers of $S_{8(S)}$ and $Li_2S_{(s)}$ particles in the simulation box (Figure 7), assist in providing insights into the reactions taking place at different stages of discharge simulations. A typical discharge curve of a conventional Li-S battery, consists of a high and a low potential plateaus with an intermediate slopy stage during which the cell potential decreases. [5,17] The cell potentials in the continuum models are derived from the current balance equation. [17,19,20] However, our kMC model does not have equations that directly relate current and potential. Therefore, here we have predicted the approximate discharge curves (Figure 6) from the concentrations of solvated particles such as $S_{4(l)}^{2-}$ and $S_{2(l)}^{2-}$ using Nernst equation [17],

$$U = U^o + \frac{RT}{2F}\left(ln\frac{c_{S_{4(l)}^{2-}}}{1000} - ln\left(\frac{c_{S_{2(l)}^{2-}}}{1000}\right)^2\right) \quad (12)$$

where U is the approximate discharge potential and U^0 is the standard potential for the $S_{4(l)}^{2-}/S_{2(l)}^{2-}$ electrochemical reaction. A similar Nernst's equation was used to predict equilibrium potentials during the discharge in a published Li-S batteries model [14].

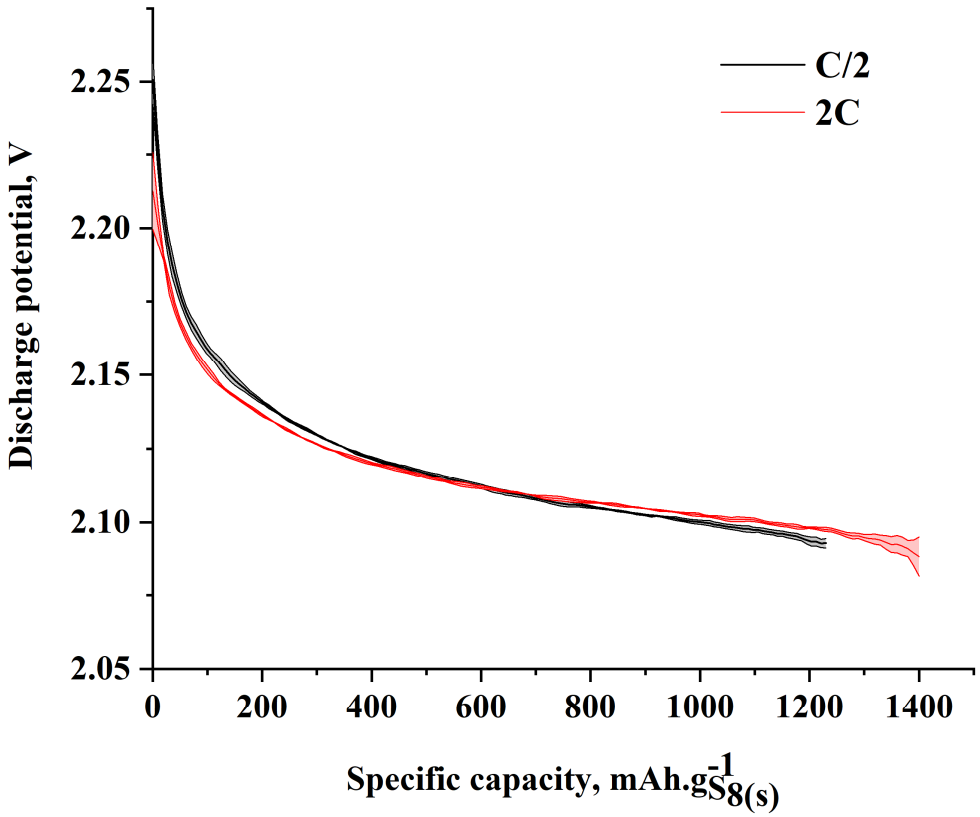

Figure 6. Approximate C/2 and 2C discharge curves – calculated using Nernst's equation for $S_{4(l)}^{2-}/S_{2(l)}^{2-}$ electrochemical reaction.

The calculated approximate discharge curves shown in Figure 6 qualitatively resemble certain experimental results with highly slopy first stage and a relatively flat second stage (see Figure S1 in the supporting information). As mentioned before, the calculated discharge curves are only used to correlate the stages of our simulations with the experiments and we did not make any attempt to predict discharge curves that quantitatively match the experimental results. Since we have used the Nernst's equation, discharge curves correspond to theoretical equilibrium potentials, which is why the variation between them are smaller in comparison with the experiments. The sensitivity of the discharge curves to the discharge rates are due to

the phenomena such as the electrolyte resistance [38], anode and cathode overpotentials [45] and transport overpotential. [20,46] Since, our kMC model simulate the discharge of a carbon/sulfur composite cathode at the mesoscopic level such phenomena are not considered in our model.

Initially, during the first slopy discharge stage, the concentrations of the solvated $S_{8(l)}$ and $S_{4(l)}^{2-}$ particles (Figure 5) increase due to the chemical dissolution of $S_{8(s)}$ particles and subsequent reduction of some $S_{8(l)}$ particles to $S_{4(l)}^{2-}$. This could be understood from the decrease in the number of $S_{8(s)}$ during this initial stage in both C/2 and 2C discharge simulations (Figure 7). However, at the midway of the first slopy discharge stage (≈100 $mAh.g_{S_{8(s)}}^{-1}$), the $S_{8(l)}$ concentrations for both C/2 and 2C simulations start to decrease (Figure 5), while the concentrations of $S_{4(l)}^{2-}$ continue to increase and those of the $S_{2(l)}^{2-}$ start to increase. This indicates that the $S_{4(l)}^{2-}/S_{2(l)}^{2-}$ reduction reaction starts at this stage in both the discharge simulations. Furthermore, the electrodeposition of $Li_2S_{(s)}$ also starts at this stage, since the numbers of $Li_2S_{(S)}$ particles for both C/2 and 2C simulations start to increase.

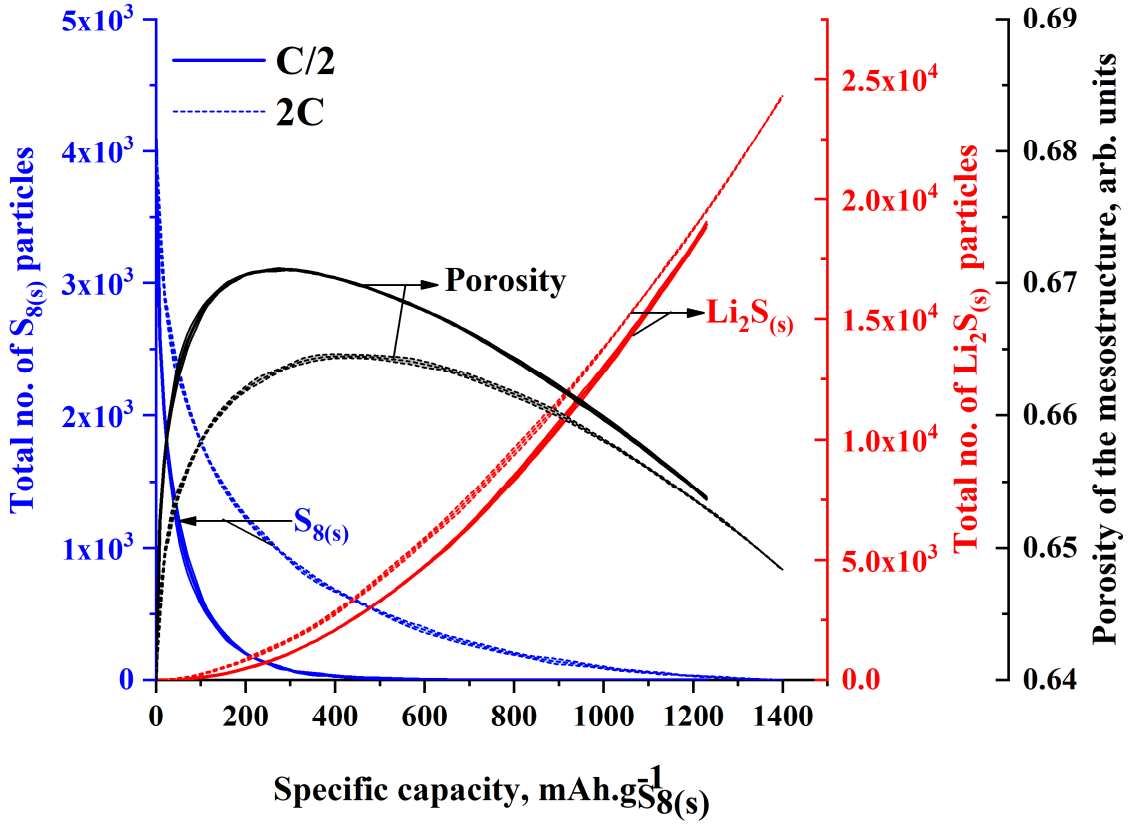

Figure 7. Evolutions of number of $S_{8(s)}$ (navy blue lines) and Li_2S (red lines) particles and the porosity of the C/S mesostructure during the C/2 (solid lines) and 2C (dashed lines) discharge simulations.

At around 250 $mAh.g^{-1}_{S_{8(s)}}$ when the approximate discharge curves start to become relatively flat – the $S^{2-}_{4(l)}$ concentrations for both simulations start to decrease, whereas the numbers of $Li_2S_{(s)}$ particles start to increase at a faster rate. This suggest that the $S^{2-}_{4(l)}/S^{2-}_{2(l)}$ and $S^{2-}_{2(l)}/Li_2S_{(s)}$ reduction reactions start to become dominant at around 250 $mAh.g^{-1}_{S_{8(s)}}$ in both the simulations. The simulated discharge curves remain relatively flat from 250 to 1200 $mAh.g^{-1}_{S_{8(s)}}$, this stage in the discharge simulations correspond to the second discharge plateau seen in experiments (Figure S1). The number of $Li_2S_{(s)}$ particles continue to increase during this relatively flat discharge stage and until the end of the simulations, whereas the

concentrations $S_{4(l)}^{2-}$ particles start to decrease at around 800 $mAh.g_{S_{8(s)}}^{-1}$, which suggest that the electrodeposition of $Li_2S_{(s)}$ particles is the most dominant reaction from this specific capacity. Since, the $S_{8(s)}$ dissolves during the slopy stage first stage of the predict discharge curve, it corresponds to the high potential plateau and slopy intermediate stage of a typical Li-S battery discharge curve.[47] Whereas, the relatively flat second stage corresponds to the low potential plateau of a typical discharge curve.[47] These trends are consistent with the numerous continuum scale simulation results.

Since the rate constant of the $Li_2S_{(s)}$ electrodeposition reaction increases with the C-rate, the number of $Li_2S_{(s)}$ particles increase slightly faster during 2C than C/2. This impact discharge rate on the precipitation rate is consistent with the continuum simulation results.[14] However, an opposite trend is observed for the decrease in the number of $S_{8(s)}$ particles (Figure 7). The rate constant for the chemical dissolution of $S_{8(s)}$ particles does not depend on the C-rate of the discharge simulation. Since the $S_{8(s)}$ particles have more time to dissolve during the C/2 discharge simulation, the number of $S_{8(s)}$ particles decreases faster with the specific capacity. Whereas, the number of $S_{8(s)}$ particles decreases very slowly with the specific capacity since $S_{8(s)}$ particles have less time to dissolve. Due to the combined effect of slow dissolution of $S_{8(s)}$ particles and fast precipitation of $Li_2S_{(s)}$ particles – the mesostructure porosity of 2C is always lower than that of the C/2 (Figure 7). However, the mesostructure porosities of both the simulations, increase during the first slopy discharge stage and decrease during the second relatively flat one, which is consistent with many of the previously reported modeling results [14,17,36]. Finally, the decrease of discharge potentials from around 1200 $mAh.g_{S_{8(s)}}^{-1}$ (Figure 6) are due to the significant depletion in the concentrations of all the solvated sulfur based particles (Figure 5).

3.2 Mesoscale evolutions of Li_2S deposits over carbon

Since the deposition of $Li_2S_{(s)}$ over the carbon surface impact the discharge performance due to the surface passivation, it is important to understand the impact of the C-rates on the evolutions of mesoscale properties.

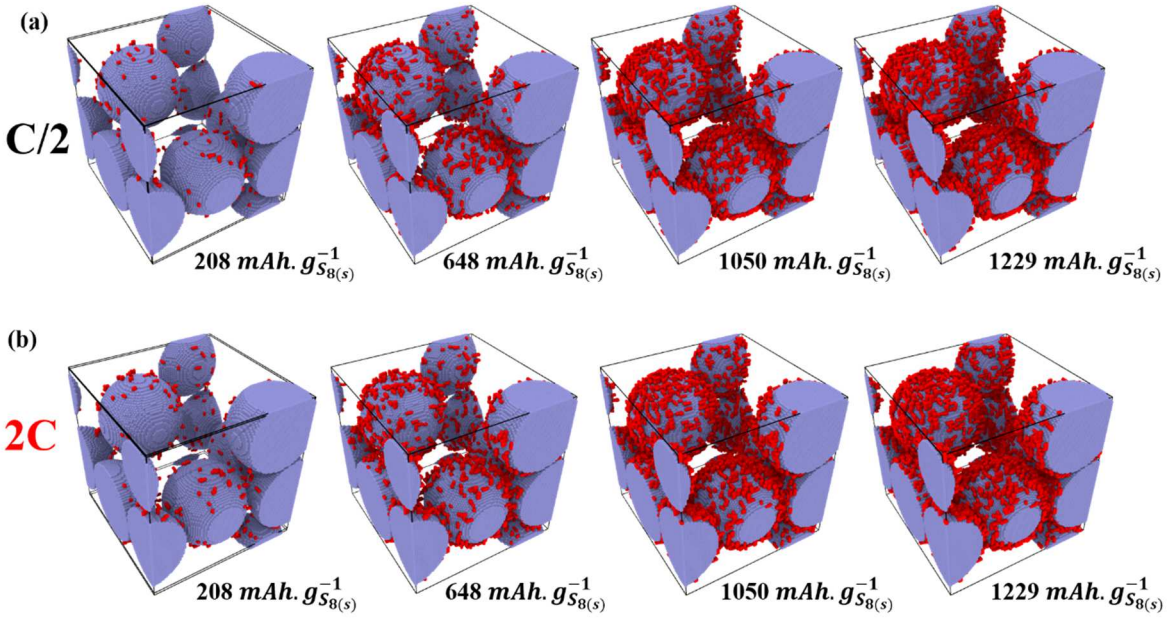

Figure 8. Visualizations of $Li_2S_{(s)}$ deposits (in red) over the surface of the carbon particles at 208, 648, 1050 and 1229 $mAh.g_{S_{8(s)}}^{-1}$ during (a) C/2 and (b) 2C discharge simulations.

The visualizations of $Li_2S_{(s)}$ deposits over the surface of carbon particles at different DoDs during C/2 and 2C (see video in the supplementary materials) discharge simulations are shown in Figure 8. Visually the evolutions $Li_2S_{(s)}$ depositions over the carbon surface look similar for both simulations. At 208 $mAh.g_{S_{8(s)}}^{-1}$ the $Li_2S_{(s)}$ deposits exist in the form isolated nuclei and then at 648 $mAh.g_{S_{8(s)}}^{-1}$ clusters of $Li_2S_{(s)}$ particles are formed, which then grow bigger along with the formation of newer clusters occur during the subsequent stages of the discharge simulations. A similar type of $Li_2S_{(s)}$ deposition process over the carbon surface was experimentally observed by Fan *et al.* [11]. However, it is difficult to make conclusions about

the impact of C-rates on the mesoscale properties of $Li_2S_{(s)}$ deposits over the carbon surface just from the visualizations. Therefore, in the following, we have presented the analysis of the post-processed results of the $Li_2S_{(S)}$ deposits produced using computational tools such as radial distribution function and cluster recognition algorithm.

3.2.1 Distribution of $Li_2S_{(s)}$ particles from the carbon surface

Due to the discrete nature of our model, we decided to approximate the radial distribution function (RDF) as a histogram of the distances between the particles and the carbon surface. Therefore, RDF assist in determining the distribution of the number of $Li_2S_{(s)}$ particles at different distances from the the carbon particles (Figure 10). At first, we used the results of the RDF to predict the coverage of $Li_2S_{(s)}$ particles over carbon surface ($\theta_{Li_2S_{(s)}}$), which quantifies the fraction of carbon surface that is directly blocked by $Li_2S_{(s)}$ and it is calculated using the following equation,

$$\theta_{Li_2S_{(s)}} = \frac{N_c^{Li_2S_{(s)}}}{N_c^T} \tag{12}$$

where, $N_c^{Li_2S_{(s)}}$ and N_c^T respectively are the number of surface C atoms covered by $Li_2S_{(s)}$ particles and the total number of surface C atoms in simulation box. It should be noted that $N_c^{Li_2S_{(s)}}$is also the number of $Li_2S_{(s)}$ particles present at 5 Å from the surface of the carbon particles, since this distance refers to the voxels that are present right next to the C atoms.

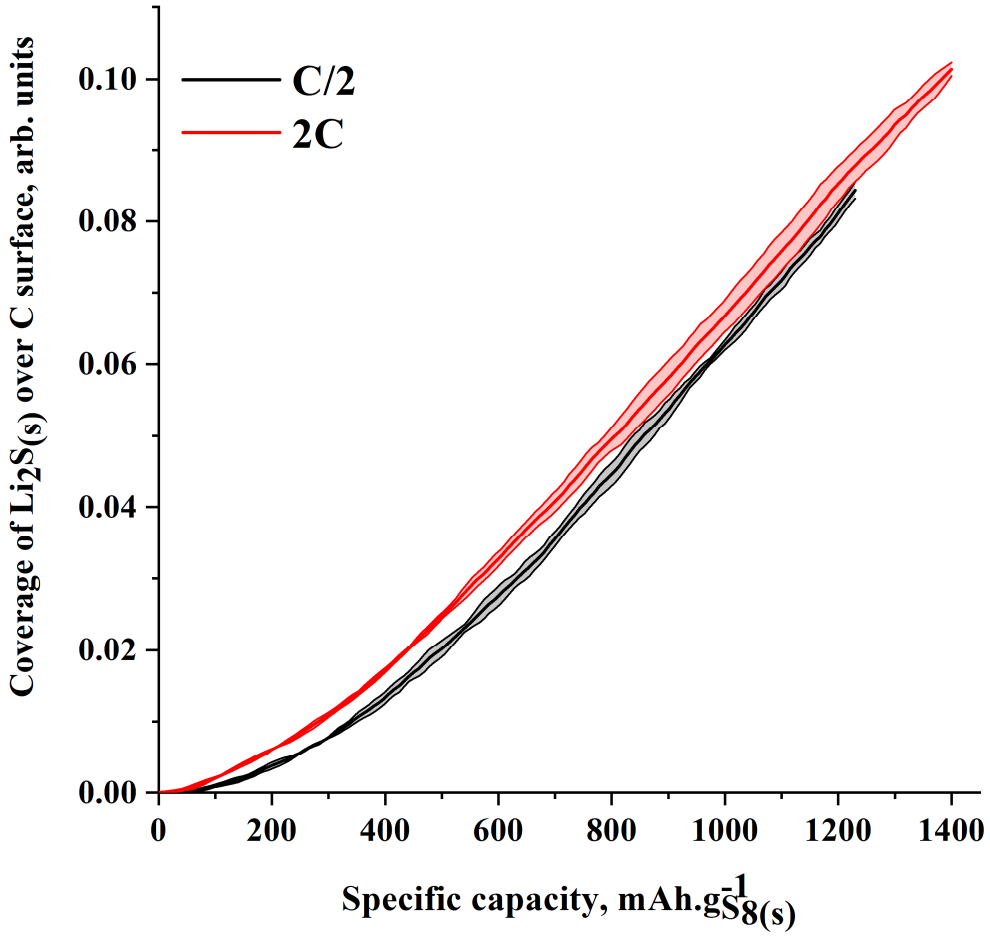

Figure 9. The evolutions of coverages of $Li_2S_{(s)}$ over carbon surface for both C/2 (black line) and 2C (red line) discharge simulations.

The increase of $Li_2S_{(s)}$ coverage over carbon surface during 2C discharge is faster than C/2 (Figure 9). This trend is consistent with the previously observed modelling results of Andrei *et al.* [13]. Furthermore, the distributions of $Li_2S_{(s)}$ particles at different distances from the carbon surface (Figure 10), show that the $Li_2S_{(s)}$ deposits, produced during both C/2 and 2C discharge simulations are multi-layered – which is a reason for the low coverages of $Li_2S_{(s)}$ over carbon surface. Although there is only a slight difference between the average numbers of $Li_2S_{(s)}$

particles produced at around 1229 $mAh.g_{S_{8(s)}}^{-1}$ during 2C and C/2 discharge simulations (Figure 7), the difference between the average coverages of $Li_2S_{(s)}$ over the carbon surface is much larger at this specific capacity (Figure 9). This suggests that the $Li_2S_{(s)}$ deposits, produced at 1229 $mAh.g_{S_{8(s)}}^{-1}$ during C/2 discharge simulation, are slightly more multi-layered than those produced during 2C. This could also be understood from the distributions of $Li_2S_{(s)}$ particles on the carbon surface at 1229 $mAh.g_{S_{8(s)}}^{-1}$ during C/2 and 2C discharge simulations (Figure 10). At this capacity, the average number of Li_2S particles present at distances beyond 2.5 nm from the carbon surface during C/2 – are slightly larger than those of the 2C.

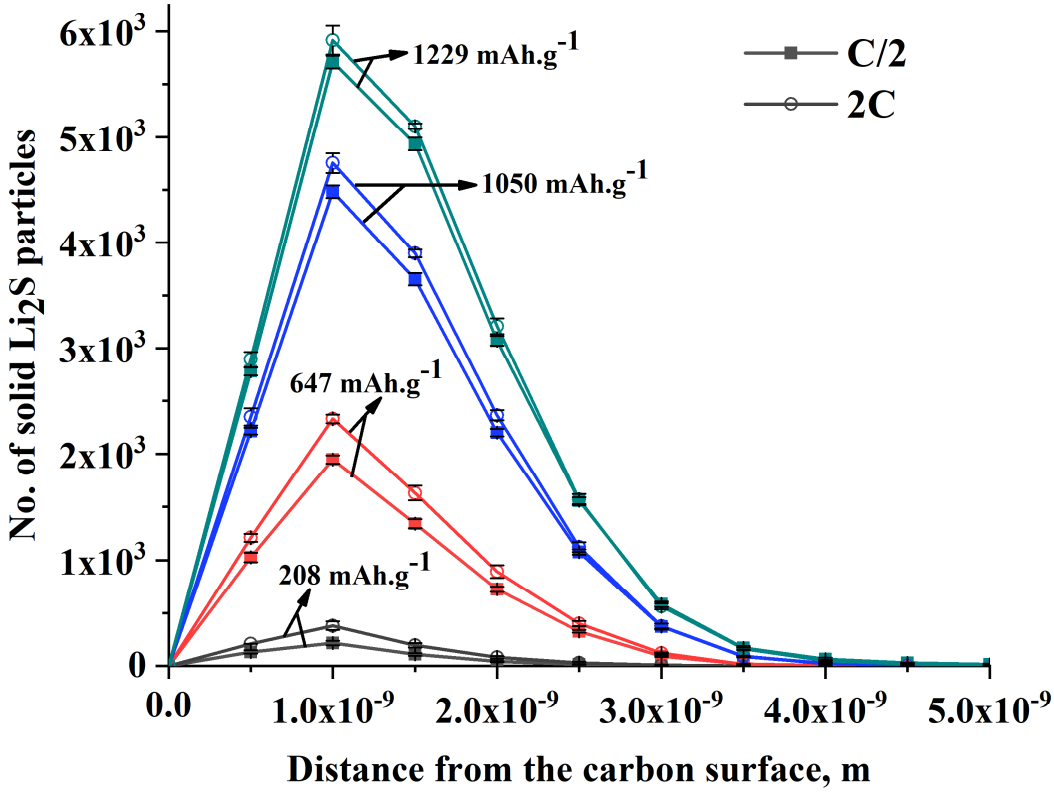

Figure 10. The distributions of $Li_2S_{(s)}$ particles at different distances from the carbon surface at 208 (grey lines), 648 (red lines), 1050 (blue lines) and 1229 (green lines) $mAh.g_{S_{8(s)}}^{-1}$ during C/2 (lines with squares) and 2C (lines with open circles) discharge simulations. The error bars in the plot are shown in black.

The impact of C-rates on the nucleation and growth dynamics of $Li_2S_{(s)}$ deposition during discharge simulations, could be understood from the comparisons of the evolutions of the $Li_2S_{(s)}$ distributions on the carbon surface (Figure 10). The peaks of all the $Li_2S_{(s)}$ distributions for the both discharge simulations – are situated at 1 nm from the carbon surface. This indicates that the $Li_2S_{(s)}$ electrodepositions during C/2 and 2C discharge simulations are dominated by the nucleation of $Li_2S_{(s)}$ deposits since they are very close to the carbon surface (Figure 10). Initially, at 208 and 648 $mAh.g_{S_{8(s)}}^{-1}$, the $Li_2S_{(s)}$ distributions of C/2 discharge simulation are all lower than those of 2C. Furthermore, at 1050 $mAh.g_{S_{8(s)}}^{-1}$ $Li_2S_{(s)}$ distributions for both C/2 and 2C discharge simulations are relatively close to each other. Moreover, the numbers of $Li_2S_{(s)}$ particles beyond 2 nm for both C/2 and 2C discharge simulations start to overlap each other at 1050 $mAh.g_{S_{8(s)}}^{-1}$ (Figure 10). Finally, at 1229 $mAh.g_{S_{8(s)}}^{-1}$, the average numbers of $Li_2S_{(s)}$ particles beyond 2.5 nm for C/2 discharge simulation are slightly larger than those of the 2C (Figure 10). These evolutions show that the broadening of distribution of $Li_2S_{(s)}$ particles over carbon during C/2 discharge is slightly faster than 2C. Therefore, this indicates that the growth process of $Li_2S_{(s)}$ deposits is slightly faster during C/2 discharge simulation, which is also consistent with the modelling predictions of Ren *et al.*[22].

Since the rate constant of the $Li_2S_{(s)}$ electrodeposition reaction increases with the C-rate, S_2^{2-} particles tend to react more when they come closer to the carbon surface during 2C than C/2

(see Figure S2 in the supplementary information). Whereas, they tend to diffuse more during C/2 than 2C. Therefore, this competition between reaction and diffusion events of S_2^{2-} particles, could be the reason – why the $Li_2S_{(s)}$ deposits of C/2 discharge simulation are more multi-layered than those of the 2C.

3.2.2 Size distribution of $Li_2S_{(s)}$ clusters

As mentioned in subsection 3.2, clusters of $Li_2S_{(s)}$ particles are formed during discharge simulations (Figure 8). The sizes of these clusters provide us details about the proximity of the $Li_2S_{(s)}$ deposits with each other. Here, the size of a cluster refers to the number of $Li_2S_{(s)}$ particles in that cluster and it assists in providing insights about the local passivation of carbon surface. Since a large $Li_2S_{(s)}$ cluster could cover a large area of the carbon surface – locally the surface passivation by that cluster will be higher than if a small cluster is formed at that same area. This local passivation of carbon surfaces could have an impact on the electrochemical performance towards the end of discharge when the concentrations of solvated polysulfides are low and unevenly distributed. Therefore, we have estimated the size distributions of $Li_2S_{(s)}$ clusters formed at $1229 mAh.\, g_{S_{8(s)}}^{-1}$ (Figure 11 and 12), using a cluster recognition algorithm called Density-base Spatial clustering of Applications with Noise (DBSCAN) [48].

DBSCAN does not require prior knowledge about the shapes and amounts of clusters, which is its main advantage over other cluster recognition algorithms. Here, we have implemented the DBSCAN algorithm in a python code and we specially adjusted it to analyse the $Li_2S_{(s)}$ particles data which were produced using our kMC code. The input parameters that DBSCAN requires are – minimum number of particles required for a region to be considered as a cluster (MinPts) and minimum distance between the particles to be considered belonging to the same

cluster (ε). In this paper, MinPts and ε were set to 5 particles and 1.5 voxel sides (7.5 Å) respectively, in order to reduce the background noise.

The visualizations and size distributions of $Li_2S_{(s)}$ clusters formed at 1229 $mAh.g_{S_{8(s)}}^{-1}$ during the both discharge simulations are shown in Figure 11 and 12. The cluster sizes vary from 4 to 367, which is too wide a range, to visualize using a single image and to represent its distribution in a single histogram. Therefore, we have classified clusters based on their cluster size classes such as 4-8, 9-13, 14-18 and so on until 39-43 $Li_2S_{(s)}$ particles per cluster (Figure 11). There are a large number of small clusters (<19) formed during both C/2 and 2C simulations. Therefore, to clearly differentiate the differences between the cluster sizes formed during C/2 and 2C discharge simulations – the visualizations and size distributions of the clusters with sizes above 43, are shown in Figure 12. Here, we classified the clusters based on the cluster size such as 44-79, 80-115, 116-151 and so on until 332-367 $Li_2S_{(s)}$ particles per cluster.

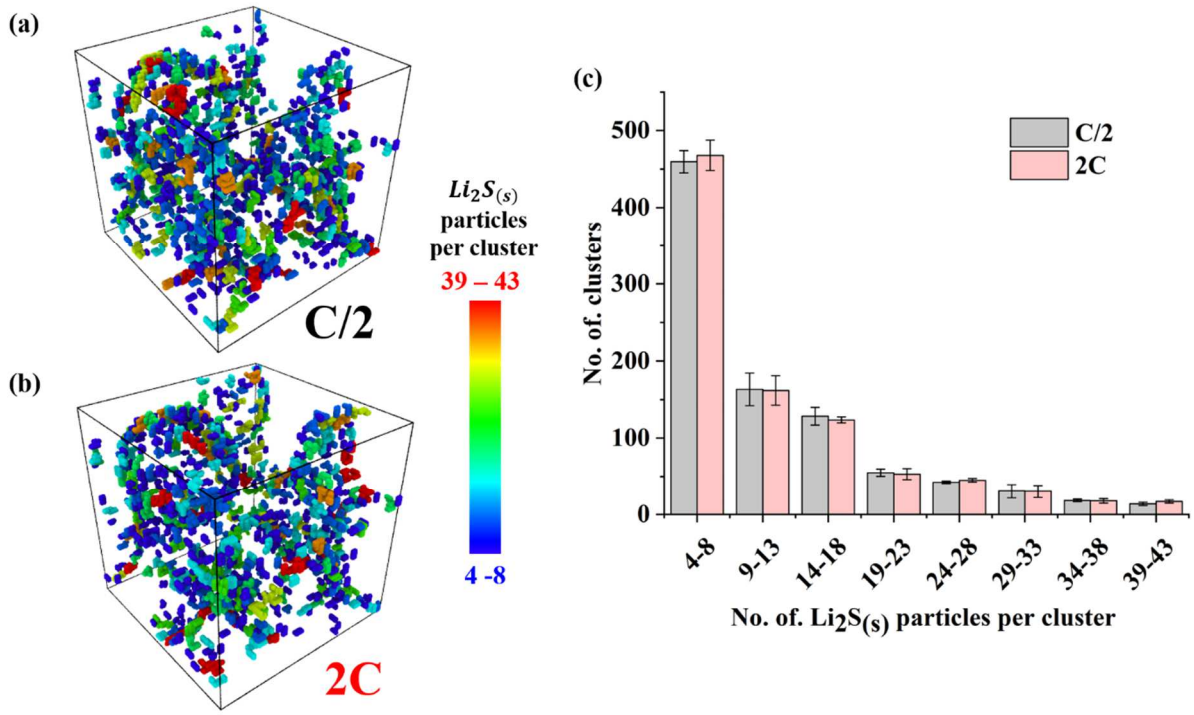

Figure 11. Visualizations of $Li_2S_{(s)}$ clusters of belonging to size classes of 4-8, 9-13, 14-18 and so on until 39-43 formed at 1229 $mAh.g_{S_{8(s)}}^{-1}$ during (a) C/2 and (b) 2C discharge simulations and (c) their corresponding cluster size distributions, where the cluster size distributions of C/2 and 2C are given in grey and pink bars respectively. The error bars over the histograms are shown in black. The colour map in the image shows the colour coding assigned to different cluster size classes (e.g. 4-8 and 39-43 are shown in navy blue and red) during visualization.

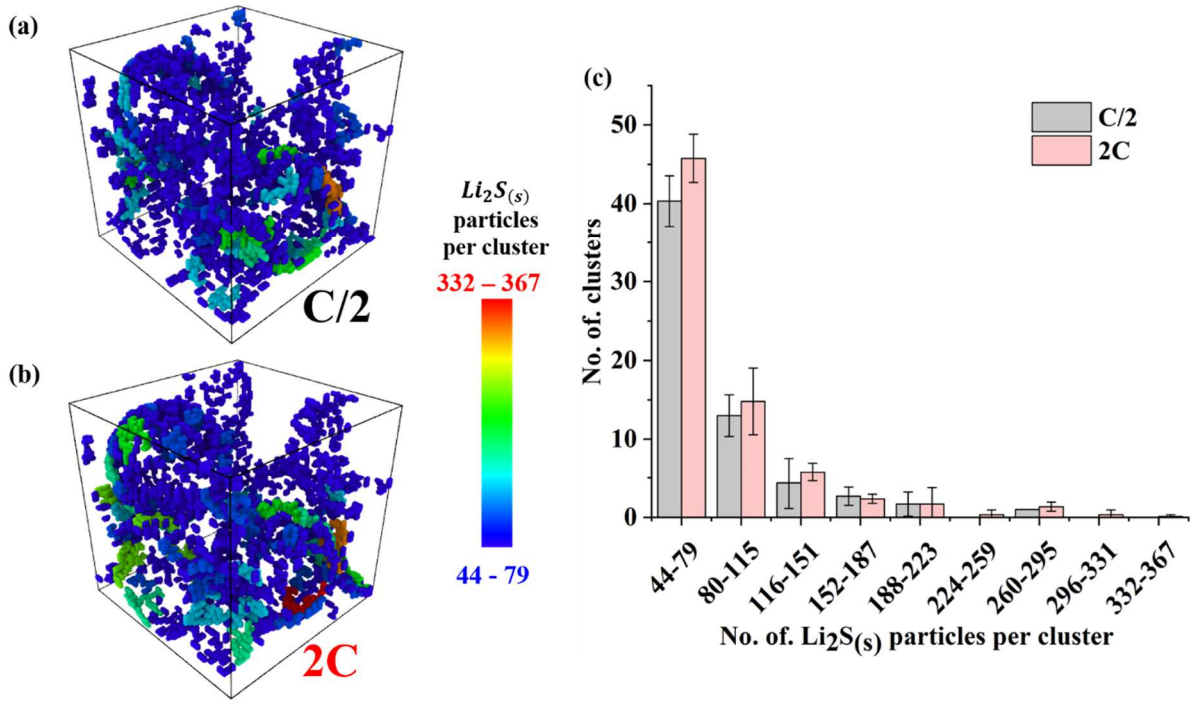

Figure 12. Visualizations of $Li_2S_{(s)}$ clusters of belonging to size classes of 44-79, 80-115, 116-151 and so on until 332-367 formed at 1229 $mAh.g_{S_{8(s)}}^{-1}$ during (a) C/2 and (b) 2C discharge simulations and (c) their corresponding cluster size distributions, where the cluster size distributions of C/2 and 2C are given in grey and pink bars respectively. The error bars over the histograms are shown in black. The colour map in the image shows the colour coding assigned to different cluster size classes (e.g. 64-94 and 95-125 are shown in navy blue and red) during visualization.

On average, the number of very small clusters (4-8) formed during 2C discharge simulation is larger than that of C/2. However, the number of $Li_2S_{(s)}$ clusters with sizes between 9 to 38 during 2C and C/2 discharge simulations are similar (Figure 11). Whereas, the average number of $Li_2S_{(s)}$ clusters produced during 2C discharge simulation – are larger in most of cluster size classes beyond 34-38. These differences between C/2 and 2C discharge simulations are more evident in cluster size classes such as 39-43 (Figure 11), 44-79, 80-115 and 116-151 (Figure 12). Therefore, we can conclude that on average relatively larger number of $Li_2S_{(s)}$ clusters with moderate (39-43) and big sizes (44-367) are formed during 2C (Figure 12).

$Li_2S_{(s)}$ clusters with big sizes represent the $Li_2S_{(s)}$ deposits which are closer to each other. Therefore, the $Li_2S_{(s)}$ deposits produced during 2C are relatively closer than those produced during 2C, which means the local passivation of carbon surfaces are relatively high for 2C. This effect could also be due to the competition between reaction and diffusion events of $S_{2(l)}^{2-}$ particles during 2C and C/2 discharge simulations. Since $S_{2(l)}^{2-}$ particles diffuse more during C/2 discharge, they get separated more from each other, which could result in isolated deposits of $Li_2S_{(s)}$.

3.3 Sensitivity of solid sulfur mass loading

This subsection presents the 2C discharge simulation results of a C/S mesostructure with 1:0.54 C/S mass ratio. The structural parameters such as the shape and size of the carbon particles, and the carbon porosity of this mesostructure are same as the one with 1:0.27 C/S mass ratio (Figure 1). Therefore, the discharge simulation results of the aforementioned C/S mesostructures (i.e. 1:0.27 and 1:0.54 C/S mass ratios) are compared to assess the impact of the sulfur loading on the overall and $Li_2S_{(s)}$ mesostructural evolutions.

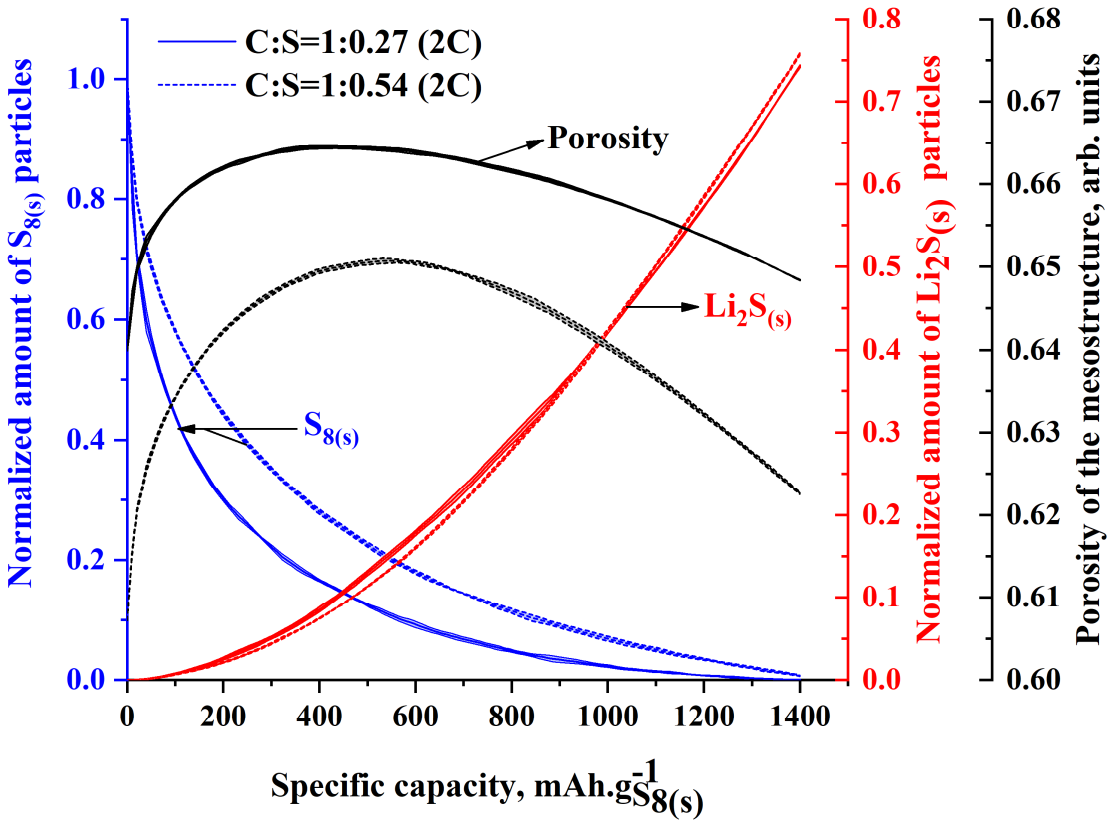

Figure 13. Evolutions of the normalized amounts of $S_{8(s)}$ (navy blue lines) and Li_2S (red lines) particles and the porosities of the C/S mesostructures with 1:0.27 (solid lines) and 1:0.54 (dashed lines) C/S mass ratios during 2C discharge simulation.

The number of S particles in the mesostructure with 1:0.54 C/S mass ratio (high-S mesostructure) is twice the low-S one (i.e. 1:0.27 C/S mass ratio). Therefore, to compare the evolution rates of $S_{8(s)}$ and $Li_2S_{(s)}$ particles in high and low-S mesostructures, we have normalized their amounts with the corresponding maximum possible number of particles (Figure 13). During discharge, the porosity of the high-S mesostructure is significantly lower

than that of the low-S one (Figure 13). This is because the absolute total number of $S_{8(s)}$ and $Li_2S_{(s)}$ particles in the high-S mesostructure are always larger than that of the low-S one.

The rate of dissolution of $S_{8(s)}$ in high-S mesostructure is slower than that of the low-S one. Since the discharge current increases with the S loading, the absolute rates of all the electrochemical reactions will also increase with it (Figure 13). Therefore, around 200 $mAh.g_{S_{8(s)}}^{-1}$ the normalized amount of $Li_2S_{(s)}$ particles in the high-S mesostructure start to increase significantly even when there is large amount undissolved $S_{8(s)}$ in it. Initially, the increase in the normalized amount of $Li_2S_{(s)}$ particles in high-S mesostructure is relative slower than that of the low-S one, which is due to the slow dissolution $S_{8(s)}$ particles. However, beyond 1000 $mAh.g_{S_{8(s)}}^{-1}$ much of the $S_{8(s)}$ particles are dissolved, therefore the rate of increase in the normalized $Li_2S_{(s)}$ particles in high-S mesostructure become relatively faster. The visual comparison of the $Li_2S_{(s)}$ deposits over the carbon surface during discharge in the mesostructures with different S-loading show that the absolute number $Li_2S_{(s)}$ particles are always higher in the high-S mesostructure (Figure 14).

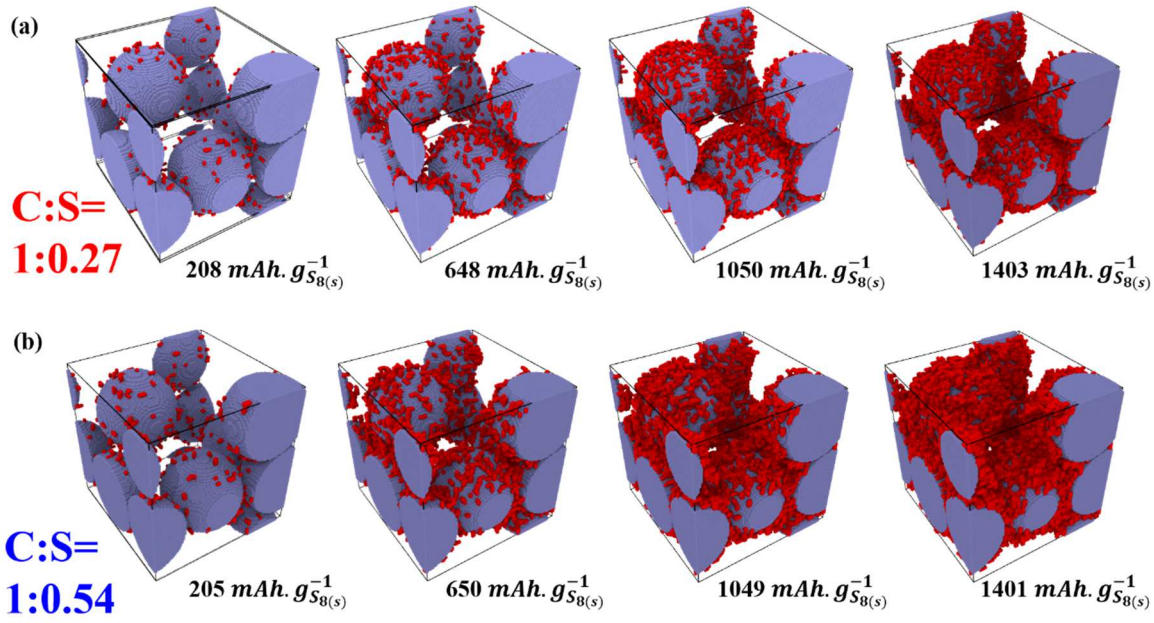

Figure 14. Visualizations of $Li_2S_{(s)}$ deposits (in red) over the surface of the carbon particles in the mesostructures with (a) 1:0.27 and (b) 1:0.54 C/S mass ratios and at different DoDs during 2C discharge simulations.

At the initial stage of discharge, the coverage of $Li_2S_{(s)}$ over the carbon surface in the high-S mesostructure increase at faster rates than that in the low-S mesostructure (Figure 15). This effect is due to the increase in the discharge current with the S loading. However, at the mid stage (≈800 $mAh.\, g_{S_{8(s)}}^{-1}$), the increase in the $Li_2S_{(s)}$ coverage in the high-S mesostructure starts to slow down (Figure 15). This is due to the low availability of free carbon surfaces, since a significant amount of the surface are covered by the previously deposited $Li_2S_{(s)}$ and undissolved $S_{8(s)}$ particles (Figure 13). Since, beyond 1000 $mAh.\, g_{S_{8(s)}}^{-1}$ the $Li_2S_{(s)}$ distributions over the carbon surface in the high-S mesostructure are significantly broader than those in the low-S one (Figure 13), they limit the transport S_2^{2-} to the carbon surface. Therefore, the $Li_2S_{(s)}$ coverage in the high-S mesostructure remain relative lower even though much of

the $S_{8(s)}$ particles are dissolved beyond this specific capacity. Ultimately, the $Li_2S_{(s)}$ coverage in high-S mesostructure at the end discharge is relatively lower than the that of the low-S one (Figure 15).

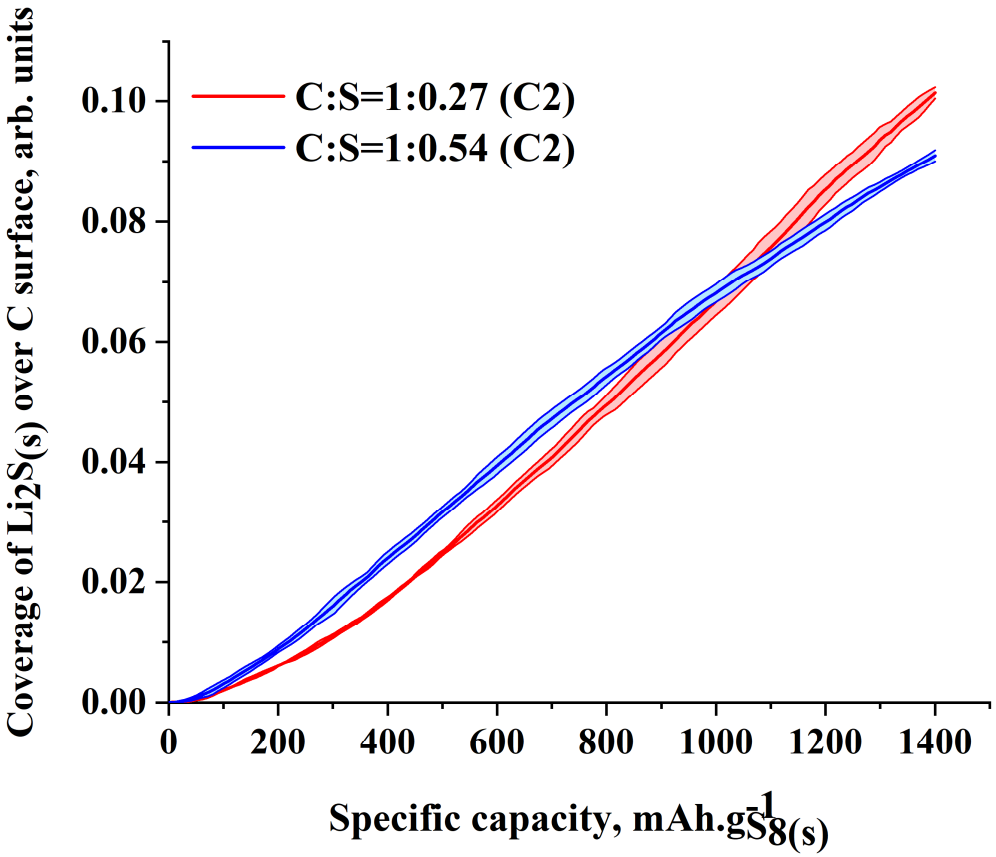

Figure 15. The evolutions of coverages of $Li_2S_{(s)}$ over carbon surface in mesostructures with 1:0.27 (red lines) and 1:0.54 (blue lines) C/S mass ratios, during 2C discharge simulations.

During discharge the peaks of the $Li_2S_{(s)}$ distributions over carbon surface in the high-S mesostructure – shift from 1.0 to 1.5 nm (Figure 16). This indicates that the growth dynamics of $Li_2S_{(s)}$ electrodeposition is more dominant than the nucleation dynamics in high-S mesostructure. This is also due to the low availability of free carbon surfaces in high-S mesostructure during discharge, since most of the surface are covered by previously deposited

$Li_2S_{(s)}$ and undissolved $S_{8(s)}$ particles. Furthermore, the slow nucleation dynamics in the high-S mesostructure is also due to the thick $Li_2S_{(s)}$ deposits over its carbon surface which limit the diffusion of S_2^{2-}.

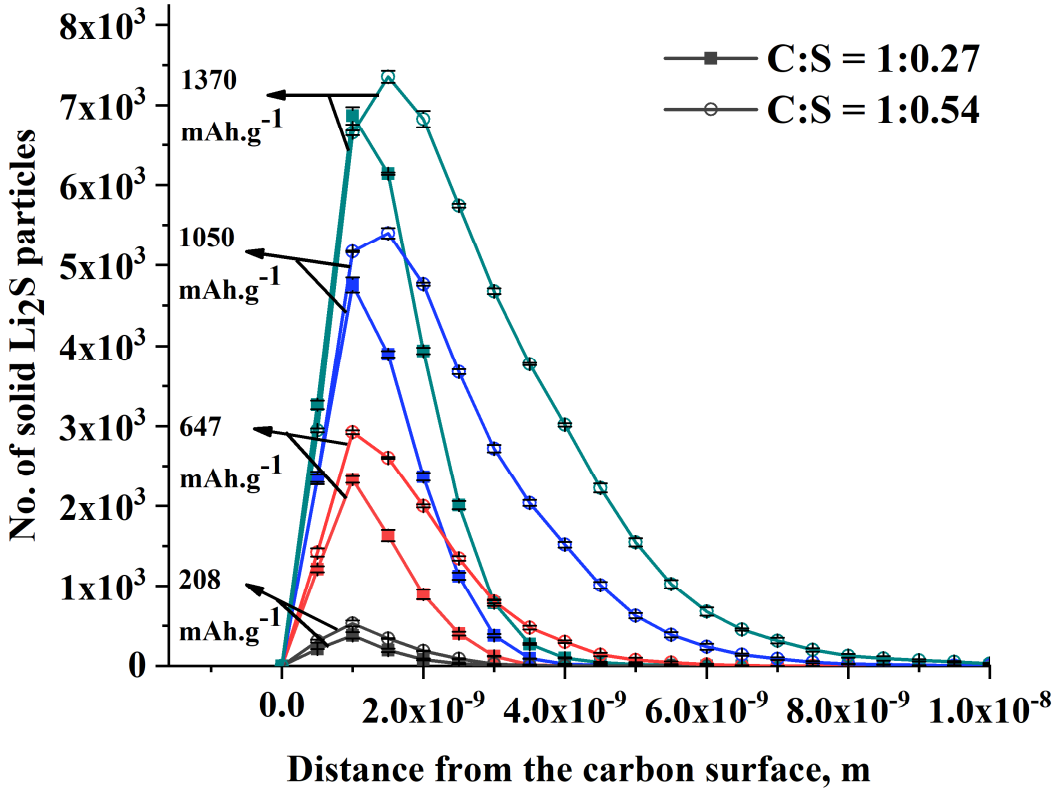

Figure 16. The distributions of $Li_2S_{(s)}$ particles at different distances from the carbon surface in the mesostructures with 1:0.27 (lines with squares) and 1:0.54 C/S (lines with open circles) mass ratio and at 208 (grey lines), 647 (red lines), 1050 (blue lines) and 1370 (green lines) $mAh.g_{S_{8(s)}}^{-1}$ during 2C discharge simulations. The error bars are shown in black.

4. Conclusion

In this paper, we presented a novel 3D kMC model which is capable of simulating the evolutions inside a C/S mesostructure during discharge. Our model can predict effective evolutions inside the mesostructure such as concentrations of solvated particle, numbers of solid sulfur based particles and mesostructure porosity. Furthermore, the approximate discharge curves calculated from the results of our kMC model, assist in assessing the phenomena taking place at different stages of discharge. The evolutions of mesostructure porosities, such as their increase during the first slopy discharge stage and decrease during the second relative flat discharge stage are consistent with the previously reported continuum modeling results [14,17,36]. Furthermore, the reduction of long chain (S_8) to medium chain polysulfide (S_4^{2-}) during the first slopy stage and subsequent reduction of S_4^{2-} to S_2^{2-} and precipitation of $Li_2S_{(s)}$ during the relatively flat stage are consistent with the continuum simulation [14,37] and experimental results. [49,50]

The post-processed results of $Li_2S_{(s)}$ data produced by the simulations our kMC model, assist in assessing the impact of C-rates on the mesoscale properties of $Li_2S_{(s)}$. The results produced using the radial distribution function, show that $Li_2S_{(s)}$ coverage over carbon increases with the C-rate, while the $Li_2S_{(s)}$ deposits formed during slow C-rate (C/2) are relatively more multi-layered. These effects are due to nucleation and growth dynamics of $Li_2S_{(s)}$ electrodepositions, where the evolutions of the distributions $Li_2S_{(s)}$ deposits on the carbon surface indicate that growth process of $Li_2S_{(s)}$ is slightly faster during slow C-rate (C/2). These aforementioned conclusions made from our kMC model are consistent with previously reported modeling and experimental results of Andrei et al. [13] and Ren *et al.* [22]. Furthermore, comparison of the size distributions of $Li_2S_{(s)}$ clusters of C/2 and 2C discharge simulations, show that relatively small number of big deposits are produced during slow discharge. This could be due to the

competition between reaction and diffusion S_2^{2-}. Due to the insulating of nature $Li_2S_{(s)}$, the mesoscale properties of its deposits over carbon will impact the surface passivation [13,23]. Since the $Li_2S_{(s)}$ coverage over carbon increases faster during fast discharge (2C), we believe that the overall surface passivation is also faster during fast discharge. Furthermore, since relatively large number of bigger clusters are formed during fast discharge, local passivation of carbon surfaces are also larger during the fast discharge. These passivation effects could be some the reasons, why the discharge capacity decreases when the C-rate increases.

The results of the radial distribution function show that the $Li_2S_{(s)}$deposits over the carbon surface in high-S mesostructure (i.e. 1:0.54 C/S mass ratio) are relative thicker than those in low-S mesostructure. This is also evident from the relatively low $Li_2S_{(s)}$ coverage over carbon surface in high-S mesostructure at the end of the 2C discharge simulation. Therefore, the growth process of the $Li_2S_{(s)}$ electrodeposition in high-S mesostructure is more dominant than the $Li_2S_{(s)}$ nucleation process. These phenomena are primarily due to the lack of free carbon surfaces during simulation in high-S mesostructure, since most of the surface is covered by previously deposited $Li_2S_{(s)}$ and undissolved $S_{8(s)}$. Due to the combined effect of thick $Li_2S_{(s)}$ deposits and coverage of undissolved $S_{8(s)}$ in high-S mesostructure – surface passivation increases significantly with the S loading. This conclusion about the impact of S loading on the surface passivation is consistent with the experimental results reported by Fan *et. al.* [12]. Furthermore, thick $Li_2S_{(s)}$deposits will also limit the transport of solvate species towards the electrode surface, which could impede the electrochemical reactions. Finally, our kMC results show that porosity of the high-S mesostructure throughout 2C discharge simulation is lower than that of the low-S mesostructure. This suggest that the possibility of pore blocking during discharge could increase with the S loading. Therefore, the increase in

the surface passivation rate and possibility of pore blocking could be some of the reasons – why the discharge capacity of Li-S batteries decreases when the S loading in the cathode is increased.

The new insights of our kMC such as the formation of $Li_2S_{(s)}$ clusters during discharge, whose impact on the active surface of the cathode may not be accurately captured by the Bruggeman relation used in most of the continuum Li-S batteries model. Our model also predicts the formation anisotropic multi-layered Li_2S deposits, therefore the overall coverage over the carbon surface will be different from those of the Li_2S particles which have identical size or narrow size range. In order to accurately capture these aforementioned effects algebraic equations which matches with the average mesostructural properties of our kMC modelling results could be implemented in the continuum models. The focus of our future work will be the sensitivity analysis of the kinetic and mesostructural parameters of our kMC model. Finally, the main disadvantage of our model is its computational cost, therefore we will also work to improve the efficiency of our kMC code, for instance through its parallelization.

Appendix A. Supplementary materials

Supporting information for this article are as follows,

- Parameters used in our kMC model, an example experimental discharge curve of a Li-S coin cell and a plot showing the number of reaction and diffusion event during discharge simulations. (DOCX)
- Video showing the overall evolution of C/S mesostructure during 2C discharge (corresponding to Figure 4). (AVI)
- Video showing the $Li_2S_{(s)}$ deposition during 2C discharge (corresponding to Figure 8). (AVI)

Data availability

The raw/processed data required to reproduce these findings cannot be shared at this time as the data also forms part of an ongoing study.

References

[1] S. Sripad, V. Viswanathan, Performance Metrics Required of Next-Generation Batteries to Make a Practical Electric Semi Truck, ACS Energy Lett. 2 (2017) 1669–1673. doi:10.1021/acsenergylett.7b00432.

[2] P.G. Bruce, S.A. Freunberger, L.J. Hardwick, J.-M. Tarascon, Li–O2 and Li–S batteries with high energy storage, Nat. Mater. 11 (2012) 19–29. doi:10.1038/nmat3191.

[3] T. Cleaver, P. Kovacik, M. Marinescu, T. Zhang, G. Offer, Perspective—Commercializing Lithium Sulfur Batteries: Are We Doing the Right Research?, J. Electrochem. Soc. 165 (2018) A6029–A6033. doi:10.1149/2.0071801jes.

[4] D. Larcher, J.-M. Tarascon, Towards greener and more sustainable batteries for electrical energy storage, Nat. Chem. 7 (2015) 19–29. doi:10.1038/nchem.2085.

[5] L.F. Nazar, M. Cuisinier, Q. Pang, Lithium-sulfur batteries, MRS Bull. 39 (2014) 436–442. doi:10.1557/mrs.2014.86.

[6] X. Ji, K.T. Lee, L.F. Nazar, A highly ordered nanostructured carbon–sulphur cathode for lithium–sulphur batteries, Nat. Mater. 8 (2009) 500–506. doi:10.1038/nmat2460.

[7] N. Jayaprakash, J. Shen, S.S. Moganty, A. Corona, L.A. Archer, Porous Hollow Carbon@Sulfur Composites for High-Power Lithium-Sulfur Batteries, Angew. Chem. 123 (2011) 6026–6030. doi:10.1002/ange.201100637.

[8] J. Schuster, G. He, B. Mandlmeier, T. Yim, K.T. Lee, T. Bein, L.F. Nazar, Spherical Ordered Mesoporous Carbon Nanoparticles with High Porosity for Lithium-Sulfur Batteries, Angew. Chem. Int. Ed. 51 (2012) 3591–3595. doi:10.1002/anie.201107817.

[9] A. Yermukhambetova, C. Tan, S.R. Daemi, Z. Bakenov, J.A. Darr, D.J.L. Brett, P.R. Shearing, Exploring 3D microstructural evolution in Li-Sulfur battery electrodes using in-situ X-ray tomography, Sci. Rep. 6 (2016). doi:10.1038/srep35291.

[10] A. Manthiram, Y. Fu, Y.-S. Su, Challenges and Prospects of Lithium–Sulfur Batteries, Acc. Chem. Res. 46 (2013) 1125–1134. doi:10.1021/ar300179v.

[11] F.Y. Fan, W.C. Carter, Y.-M. Chiang, Mechanism and Kinetics of Li_2S Precipitation in Lithium-Sulfur Batteries, Adv. Mater. 27 (2015) 5203–5209. doi:10.1002/adma.201501559.

[12] F.Y. Fan, Y.-M. Chiang, Electrodeposition Kinetics in Li-S Batteries: Effects of Low Electrolyte/Sulfur Ratios and Deposition Surface Composition, J. Electrochem. Soc. 164 (2017) A917–A922. doi:10.1149/2.0051706jes.

[13] P. Andrei, C. Shen, J.P. Zheng, Theoretical and experimental analysis of precipitation and solubility effects in lithium-sulfur batteries, Electrochimica Acta. 284 (2018) 469–484. doi:10.1016/j.electacta.2018.07.045.

[14] V. Thangavel, K.-H. Xue, Y. Mammeri, M. Quiroga, A. Mastouri, C. Guéry, P. Johansson, M. Morcrette, A.A. Franco, A Microstructurally Resolved Model for Li-S Batteries Assessing the Impact of the Cathode Design on the Discharge Performance, J. Electrochem. Soc. 163 (2016) A2817–A2829. doi:10.1149/2.0051614jes.

[15] X. Chen, T. Hou, K.A. Persson, Q. Zhang, Combining theory and experiment in lithium–sulfur batteries: Current progress and future perspectives, Mater. Today. 22 (2019) 142–158. doi:10.1016/j.mattod.2018.04.007.
[16] A.A. Franco, Chapter 8: Computational Modeling of Lithium–Sulfur Batteries: Myths, Facts, and Controversies, in: R. Demir-Cakan (Ed.), Li- Batter. Chall. Chem. Mater. Future Perspect., WORLD SCIENTIFIC (EUROPE), London, 2017: pp. 335–350. doi:10.1142/9781786342508_0008.
[17] K. Kumaresan, Y. Mikhaylik, R.E. White, A Mathematical Model for a Lithium–Sulfur Cell, J. Electrochem. Soc. 155 (2008) A576–A582. doi:10.1149/1.2937304.
[18] T. Zhang, M. Marinescu, L. O'Neill, M. Wild, G. Offer, Modeling the voltage loss mechanisms in lithium–sulfur cells: the importance of electrolyte resistance and precipitation kinetics, Phys. Chem. Chem. Phys. 17 (2015) 22581–22586. doi:10.1039/C5CP03566J.
[19] A.F. Hofmann, D.N. Fronczek, W.G. Bessler, Mechanistic modeling of polysulfide shuttle and capacity loss in lithium–sulfur batteries, J. Power Sources. 259 (2014) 300–310. doi:10.1016/j.jpowsour.2014.02.082.
[20] T. Zhang, M. Marinescu, S. Walus, G.J. Offer, Modelling transport-limited discharge capacity of lithium-sulfur cells, Electrochimica Acta. 219 (2016) 502–508. doi:10.1016/j.electacta.2016.10.032.
[21] T. Zhang, M. Marinescu, S. Walus, P. Kovacik, G.J. Offer, What Limits the Rate Capability of Li-S Batteries during Discharge: Charge Transfer or Mass Transfer?, J. Electrochem. Soc. 165 (2018) A6001–A6004.
[22] Y.X. Ren, T.S. Zhao, M. Liu, P. Tan, Y.K. Zeng, Modeling of lithium-sulfur batteries incorporating the effect of Li2S precipitation, J. Power Sources. 336 (2016) 115–125. doi:10.1016/j.jpowsour.2016.10.063.
[23] A. Mistry, P.P. Mukherjee, Precipitation–Microstructure Interactions in the Li-Sulfur Battery Electrode, J. Phys. Chem. C. 121 (2017) 26256–26264. doi:10.1021/acs.jpcc.7b09997.
[24] S. Perez Beltran, P.B. Balbuena, Formation of Multilayer Graphene Domains with Strong Sulfur-Carbon Interaction and Enhanced Sulfur Reduction Zones for Lithium-Sulfur Battery Cathodes, ChemSusChem. 11 (2018) 1970–1980. doi:10.1002/cssc.201702446.
[25] G. Blanquer, Y. Yin, M.A. Quiroga, A.A. Franco, Modeling Investigation of the Local Electrochemistry in Lithium-O_2 Batteries: A Kinetic Monte Carlo Approach, J. Electrochem. Soc. 163 (2016) A329–A337. doi:10.1149/2.0841602jes.
[26] Y. Yin, R. Zhao, Y. Deng, A.A. Franco, Compactness of the Lithium Peroxide Thin Film Formed in Li–O_2 Batteries and Its Link to the Charge Transport Mechanism: Insights from Stochastic Simulations, J. Phys. Chem. Lett. 8 (2017) 599–604. doi:10.1021/acs.jpclett.6b02732.
[27] G. Shukla, D. del Olmo Diaz, V. Thangavel, A.A. Franco, Self-Organization of Electroactive Suspensions in Discharging Slurry Batteries: A Mesoscale Modeling Investigation, ACS Appl. Mater. Interfaces. 9 (2017) 17882–17889. doi:10.1021/acsami.7b02567.
[28] Z. Liu, P.P. Mukherjee, Mesoscale Elucidation of Surface Passivation in the Li–Sulfur Battery Cathode, ACS Appl. Mater. Interfaces. 9 (2017) 5263–5271. doi:10.1021/acsami.6b15066.
[29] A. Stukowski, Visualization and analysis of atomistic simulation data with OVITO–the Open Visualization Tool, Model. Simul. Mater. Sci. Eng. 18 (2010) 015012. doi:10.1088/0965-0393/18/1/015012.

[30] Y. Ma, H. Zhang, B. Wu, M. Wang, X. Li, H. Zhang, Lithium Sulfur Primary Battery with Super High Energy Density: Based on the Cauliflower-like Structured C/S Cathode, Sci. Rep. 5 (2015) 14949. doi:10.1038/srep14949.
[31] J. Zheng, M. Gu, M.J. Wagner, K.A. Hays, X. Li, P. Zuo, C. Wang, J.-G. Zhang, J. Liu, J. Xiao, Revisit Carbon/Sulfur Composite for Li-S Batteries, J. Electrochem. Soc. 160 (2013) A1624–A1628. doi:10.1149/2.013310jes.
[32] M.A. Quiroga, A.A. Franco, A Multi-Paradigm Computational Model of Materials Electrochemical Reactivity for Energy Conversion and Storage, J. Electrochem. Soc. 162 (2015) E73–E83. doi:10.1149/2.1011506jes.
[33] G. Shukla, A.A. Franco, Handling Complexity of Semisolid Redox Flow Battery Operation Principles through Mechanistic Simulations, J. Phys. Chem. C. 122 (2018) 23867–23877. doi:10.1021/acs.jpcc.8b06642.
[34] M. Marinescu, T. Zhang, G.J. Offer, A zero dimensional model of lithium–sulfur batteries during charge and discharge, Phys. Chem. Chem. Phys. 18 (2016) 584–593. doi:10.1039/C5CP05755H.
[35] T. Danner, G. Zhu, A.F. Hofmann, A. Latz, Modeling of nano-structured cathodes for improved lithium-sulfur batteries, Electrochimica Acta. 184 (2015) 124–133. doi:10.1016/j.electacta.2015.09.143.
[36] A.D. Dysart, J.C. Burgos, A. Mistry, C.-F. Chen, Z. Liu, C.N. Hong, P.B. Balbuena, P.P. Mukherjee, V.G. Pol, Towards next generation lithium-sulfur batteries: non-conventional carbon compartments/sulfur electrodes and multi-scale analysis, J. Electrochem. Soc. 163 (2016) A730–A741. doi:10.1149/2.0481605jes.
[37] Y.X. Ren, T.S. Zhao, M. Liu, P. Tan, Y.K. Zeng, Modeling of lithium-sulfur batteries incorporating the effect of Li2S precipitation, J. Power Sources. 336 (2016) 115–125. doi:10.1016/j.jpowsour.2016.10.063.
[38] T. Zhang, M. Marinescu, L. O'Neill, M. Wild, G. Offer, Modeling the voltage loss mechanisms in lithium–sulfur cells: the importance of electrolyte resistance and precipitation kinetics, Phys. Chem. Chem. Phys. 17 (2015) 22581–22586. doi:10.1039/C5CP03566J.
[39] Z. Li, Y. Zhou, Y. Wang, Y.-C. Lu, Solvent-Mediated Li $_2$ S Electrodeposition: A Critical Manipulator in Lithium-Sulfur Batteries, Adv. Energy Mater. 9 (2019) 1802207. doi:10.1002/aenm.201802207.
[40] F.Y. Fan, W.C. Carter, Y.-M. Chiang, Mechanism and Kinetics of Li $_2$ S Precipitation in Lithium-Sulfur Batteries, Adv. Mater. 27 (2015) 5203–5209. doi:10.1002/adma.201501559.
[41] A. Bewick, M. Fleischmann, H.R. Thirsk, Kinetics of the electrocrystallization of thin films of calomel, Trans. Faraday Soc. 58 (1962) 2200. doi:10.1039/tf9625802200.
[42] M. Jafarian, M.G. Mahjani, F. Gobal, I. Danaee, Effect of potential on the early stage of nucleation and growth during aluminum electrocrystallization from molten salt (AlCl3–NaCl–KCl), J. Electroanal. Chem. 588 (2006) 190–196. doi:10.1016/j.jelechem.2005.12.028.
[43] H. Park, N. Kumar, M. Melander, T. Vegge, J.M. Garcia Lastra, D.J. Siegel, Adiabatic and Nonadiabatic Charge Transport in Li–S Batteries, Chem. Mater. 30 (2018) 915–928. doi:10.1021/acs.chemmater.7b04618.
[44] E. Markevich, G. Salitra, Y. Talyosef, F. Chesneau, D. Aurbach, Review—On the Mechanism of Quasi-Solid-State Lithiation of Sulfur Encapsulated in Microporous Carbons: Is the Existence of Small Sulfur Molecules Necessary?, J. Electrochem. Soc. 164 (2017) A6244–A6253. doi:10.1149/2.0391701jes.

[45] M. Ghaznavi, P. Chen, Sensitivity analysis of a mathematical model of lithium–sulfur cells part I: Applied discharge current and cathode conductivity, J. Power Sources. 257 (2014) 394–401. doi:10.1016/j.jpowsour.2013.10.135.
[46] T. Zhang, M. Marinescu, S. Walus, P. Kovacik, G.J. Offer, What Limits the Rate Capability of Li-S Batteries during Discharge: Charge Transfer or Mass Transfer?, J. Electrochem. Soc. 165 (2018) A6001–A6004.
[47] S. Waluś, C. Barchasz, R. Bouchet, J.-C. Leprêtre, J.-F. Colin, J.-F. Martin, E. Elkaïm, C. Baehtz, F. Alloin, Lithium/Sulfur Batteries Upon Cycling: Structural Modifications and Species Quantification by In Situ and Operando X-Ray Diffraction Spectroscopy, Adv. Energy Mater. 5 (2015) 1500165. doi:10.1002/aenm.201500165.
[48] M. Ester, H.-P. Kriegel, J. Sander, X. Xu, CiteSeerX — A density-based algorithm for discovering clusters in large spatial databases with noise, (n.d.). https://citeseerx.ist.psu.edu/viewdoc/summary?doi=10.1.1.121.9220 (accessed February 5, 2019).
[49] A. Kawase, S. Shirai, Y. Yamoto, R. Arakawa, T. Takata, Electrochemical reactions of lithium–sulfur batteries: an analytical study using the organic conversion technique, Phys Chem Chem Phys. 16 (2014) 9344–9350. doi:10.1039/C4CP00958D.
[50] M. Cuisinier, P.-E. Cabelguen, S. Evers, G. He, M. Kolbeck, A. Garsuch, T. Bolin, M. Balasubramanian, L.F. Nazar, Sulfur Speciation in Li–S Batteries Determined by Operando X-ray Absorption Spectroscopy, J. Phys. Chem. Lett. 4 (2013) 3227–3232. doi:10.1021/jz401763d.

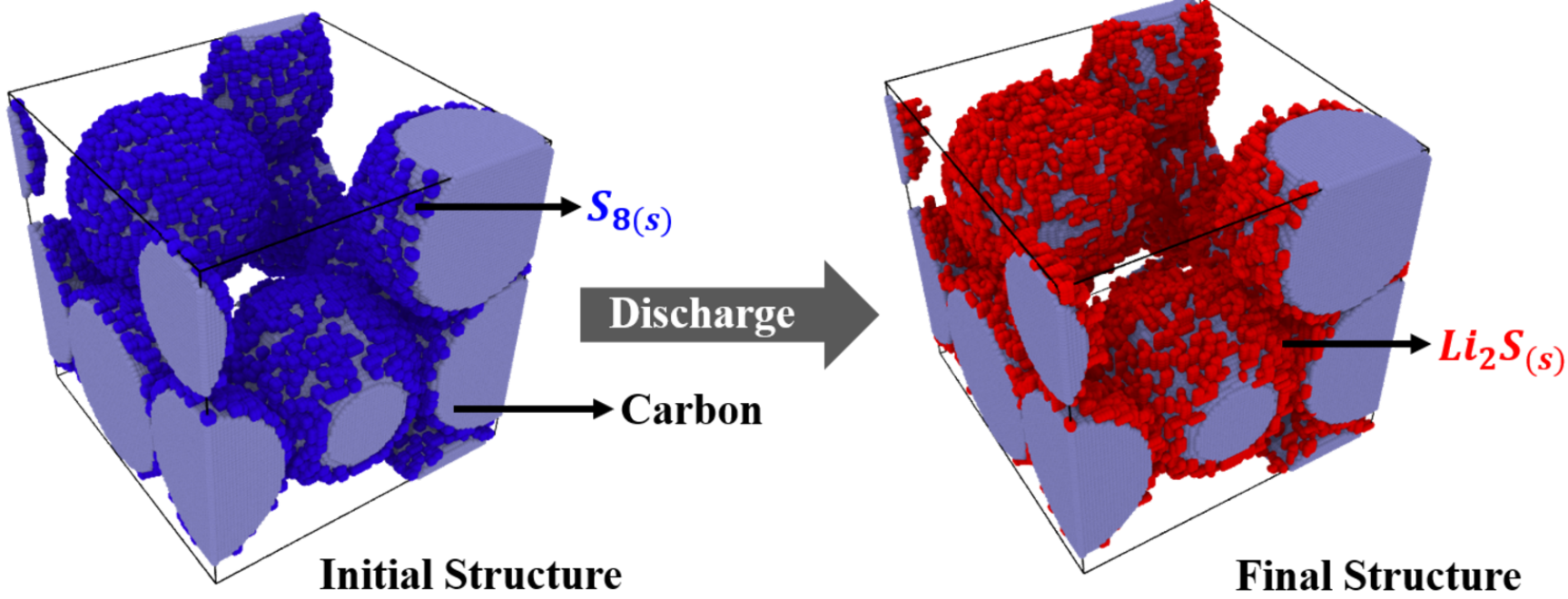
$S_{8(s)}$
Carbon
Discharge
$Li_2S_{(s)}$
Initial Structure
Final Structure

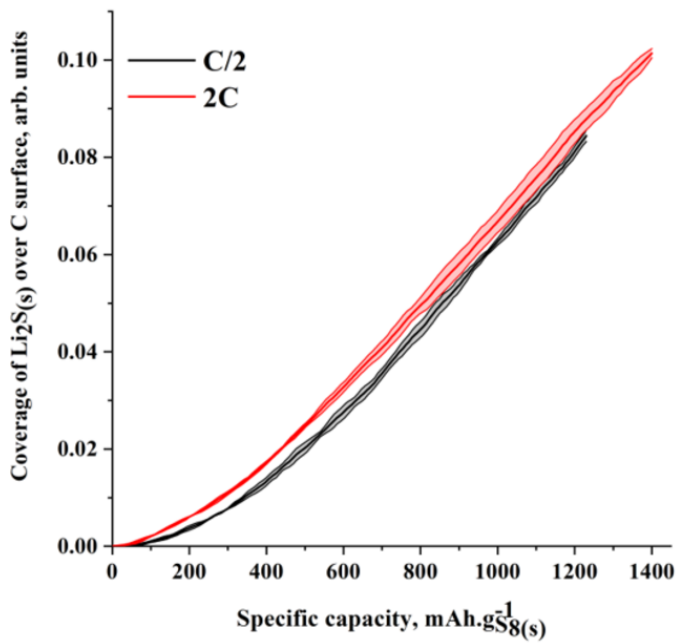
C/2
2C
Coverage of Li2S(s) over C surface, arb. units
0.00
0.02
0.04
0.06
0.08
0.10
0
200
400
600
800
1000
1200
1400
Specific capacity, mAh.gS8(s)-1